Nano Research

ISSN 1998-0124 CN 11-5974/O4
https://doi.org/10.26599/NR.2026.94909264

Research Article

Neighboring Rh nanoclusters promote the activity and stability of Rh single-atom catalyst for the hydroformylation of sterically hindered diisobutylene

Pengzhen Yin[1,4,§], Chao Feng[2,§], Shingo Hasegawa[3], Ken Motokura[3], Yifan Liu[1,4], Yi Zhang[1], Yudi Wu[1], Zhaozhan Wang[1,5], Yong Yang[1,4,5](✉)

[1] Key Laboratory of Photoelectric Conversion and Utilization of Solar Energy, Qingdao Institute of Bioenergy and Bioprocess Technology, Chinese Academy of Sciences, Qingdao 266101, China

[2] College of Chemical and Biological Engineering, Shandong University of Science and Technology, Qingdao 266590, China

[3] Department of Chemistry and Life Science, Yokohama National University, Yokohama 20-8501, Japan

[4] University of Chinese Academy of Sciences, Beijing 100049, China

[5] Present address: College of Chemical Engineering, Qingdao University of Science and Technology, Qingdao 266042, China

[§] Pengzhen Yin and Chao Feng contributed equally to this work.

Nano Res., **Just Accepted Manuscript** • https://doi.org/10.26599/NR.2026.94909264

https://www.sciopen.com/journal/1998-0124 on Oct. 15, 2026

© The Authors(s)

Just Accepted

This is a "Just Accepted" manuscript, which has been examined by the peer-review process and has been accepted for publication. A "Just Accepted" manuscript is published online shortly after its acceptance,which is prior to technical editing and formatting and author proofing. Tsinghua University Press (TUP) provides "Just Accepted" as an optional and free service which allows authors to make their results available to the research community as soon as possible after acceptance. After a manuscript has been technically edited and formatted, and the page proofs have been corrected, it will be removed from the "Just Accepted" web site and published officially with volume and article number (e.g., *Nano Research*, **2025**, *18*, 94906990). Please note that technical editing may introduce minor changes to the manuscript text and/or graphics which may affect the content, and all legal disclaimers that apply to the journal pertain. In no event shall TUP be held responsible for errors or consequences arising from the use of any information contained in these "Just Accepted" manuscripts. To cite this anuscript please use its Digital Object Identifier (DOI®),which is identical for all formats of publication.

Research Article

Neighboring Rh nanoclusters promote the activity and stability of Rh single-atom catalyst for the hydroformylation of sterically hindered diisobutylene

Pengzhen Yin[1,4,§], Chao Feng[2,§], Shingo Hasegawa[3], Ken Motokura[3], Yifan Liu[1,4], Yi Zhang[1], Yudi Wu[1], Zhaozhan Wang[1,5], Yong Yang[1,4,5]*

[1] *Key Laboratory of Photoelectric Conversion and Utilization of Solar Energy, Qingdao Institute of Bioenergy and Bioprocess Technology, Chinese Academy of Sciences, Qingdao 266101, China*

[2] *College of Chemical and Biological Engineering, Shandong University of Science and Technology, Qingdao 266590, China*

[3] *Department of Chemistry and Life Science, Yokohama National University, Yokohama 20-8501, Japan*

[4] *University of Chinese Academy of Sciences, Beijing 100049, China*

[5] *Present address: College of Chemical Engineering, Qingdao University of Science and Technology, Qingdao 266042, China*

[§] *Pengzhen Yin and Chao Feng contributed equally to this work.*

Received: 28 September 2026; **Revised:** 13 October 2026; **Accepted:** 15 October 2026

Address correspondence to yangyong@qibebt.ac.cn, yangyong@qust.edu.cn

Cite this article: *Nano Research*, 2026, 19, 94909264 https://doi.org/10.26599/NR.2026.94909264

Just Accepted

Abstract: Developing efficient and leaching-resistant heterogeneous Rh catalysts for the hydroformylation of sterically hindered olefins remains a formidable challenge. Herein, we report a ligand-free heterogeneous Rh catalyst (Rh/N-AC-T), featuring a proximal dual-active-site architecture, in which Rh single atoms and nanoclusters are co-anchored on nitrogen-doped carbon (Rh/N-AC-T). The optimized Rh/N-AC-650 catalyst exhibits outstanding catalytic performance in the hydroformylation of diisobutylene (DIB), delivering high catalytic activity, excellent structural stability, and negligible Rh leaching during continuous-flow operation for over 200 h. Comprehensive spectroscopic characterizations combined with density functional theory calculations suggest that the intimate coupling between adjacent Rh single atoms and nanoclusters modulates the Rh electronic structure and the adsorption balance of H_2 , DIB, and CO. The dual-site interface facilitates H_2 activation and lower the relative energy barrier for the rate-determining CO-insertion step, accounting for the enhanced hydroformylation performance. Meanwhile, pyridinic N species within the carbon framework benefit for the stronger interactions between Rh species and support, thereby helping suppress Rh aggregation and leaching under harsh reaction conditions. This work establishes proximal Rh single atom-nanocluster dual sites as an effective design strategy for constructing high-performance, ligand-free heterogeneous catalysts for challenging carbonylation reactions.

Keywords: hydroformylation, ligand-free heterogeneous Rh catalyst, synergistic catalysis, sterically hindered olefins, single atoms

Just Accepted

1 Introduction

The hydroformylation of olefins has evolved into a cornerstone industrial process for the synthesis of C_{1+} aldehydes and their derivatives, including alcohols, acids, amines, and esters, with a global annual production capacity exceeding 12 million tons. [1,2] Industrially, hydroformylation relies predominantly on homogeneous Rh catalysts modified with phosphine ligands. [3] Although these catalysts exhibit superior activity and high chemo- and regioselectivity, their industrial application is often hampered by the arduous separation and the inherent instability of organic phosphine ligands, leading to the loss of expensive Rh and the generation of phosphorous-containing waste streams. [4] The challenge is further intensified when dealing with sterically hindered olefins, such as diisobutylene (DIB), due to their sluggish kinetics and requirement of harsh reaction conditions. In response, significant efforts have been dedicated to developing high-performance heterogeneous catalysts, motivated by their practical advantages such as ease of separation and recyclability, with the ultimate goal of transitioning from traditional molecular Rh catalysts to heterogeneous systems. These efforts include the encapsulation of well-defined Rh complexes on the porous materials, [5-7] Rh grafted to phosphine-modified porous organic polymers, [8,9] Rh complexes dissolved in non-volatile ionic liquid supported on solid carriers, [10] and the formation of solid Rh phosphides. [11] Notwithstanding these advances, the heterogeneous catalysts obtained through these approaches generally suffer from a significant decline in catalytic performance relative to their homogeneous analogues and still require expensive and air/moisture-sensitive phosphine ligands.

Alternatively, great effort has been devoted to fabricating ligand-free Rh heterogeneous catalysts to circumvent the use of phosphine ligands. As a result, a number of supported heterogeneous catalysts have been reported by dispersing or encapsulating Rh species (e.g., single atoms, nanoclusters, nanoparticles, and alloys) on or into a solid support such as porous silicas, [12-14] metal oxides, [15-17] zeolites, [18-21] and

Just Accepted

others. [22] In particular, downsizing Rh nanoparticles to nanocluster or even single-atom level led to unexpected results. For instance, Zhang and co-authors reported a seminal work on hydroformylation catalyzed by a Rh SAC supported on ZnO, which achieves catalytic efficiency comparable to that of the industrial homogeneous Wilkinson complex, $RhCl(PPh_3)_3$, attributable to its maximally exposed Rh sites with high atom utilization efficiency. [17] Liu and co-workers developed Rh nanoclusters confined within the straight channels of MFI zeolites [18,20], which demonstrated not only higher catalytic activity but also markedly enhanced linear aldehyde selectivity for long-chain α-olefins, with a linear to branched aldehyde ratio (l/b) exceeding 400, attributed to the unique spatial confinement effect of the zeolite channels. [23,24]

Despite such impressive outcomes, the hydroformylation of sterically hindered DIB and others over supported Rh single atoms or nanoclusters remains underexplored. Furthermore, unlike homogeneous Rh catalysts, which possess high conformational flexibility in solution, the hydroformylation reaction at isolated Rh sites on a support surface occurs with very limited flexibility, rendering it particularly challenging for sterically hindered olefins due to the lack of ensemble effect and large steric hindrance. Likewise, the potential of zeolite-confined Rh nanoclusters for such sterically demanding olefins remains questionable given the intrinsic size and shape selectivity of zeolites. Moreover, the stability of these Rh single atoms and nanoclusters remains a critical concern, [25,26] as they are susceptible to aggregation and leaching under the harsh conditions of carbonylation, leading to performance degradation. These stability issues are expected to be even more pronounced in the hydroformylation of sterically hindered olefins, because much harsher reaction conditions than those required for simple α-olefins are often necessary to achieve satisfactory performance. Therefore, the development of stable, high-performance ligand-free heterogeneous Rh catalysts is highly desirable for advancing DIB hydroformylation.

Just Accepted

As an important C8 olefin intermediate, DIB consists of two isomers of 2,4,4-trimethyl-1-pentene and 2,4,4-trimethyl-2-pentene, typically in an approximate 80:20 mass ratio. [27,28] Industrially, DIB is produced via acid-catalyzed dimerization of isobutene, an abundant C4 feedstock with a global annual production capacity of 4.0 million tons and a market value of around $4.1 billion derived from refineries or steam cracking operations. [29] Upgrading DIB into higher-value derivatives is therefore of significant industrial importance, as it not only extends the downstream C4 value chain but also enables the production of high-performance products such as specialty lubricants, fuel additives, and plasticizers, thereby maximizing resource utilization and economic efficiency. Hydroformylation represents one of the most important routes for converting DIB into value-added, highly branched isononanal (INA, 3,5,5-trimethylhexanal), a key intermediate that can be further hydrogenated to isononanol or oxidized to isononanoic acid. These derivatives serve as essential precursors for high-performance plasticizers, pharmaceuticals, fragrances, cosmetics, and advanced refrigeration lubricants, meeting the growing demand in the specialty chemicals market. [30] However, DIB exhibits significant steric hindrance stemming from its highly branched structure and the presence of both terminal and internal C-C double bonds, which endows it with distinctly different reactivity toward hydroformylation. This structural complexity not only limits substrate accessibility to the catalytic active site but also imposes stringent requirements on the catalyst's geometry and electronic properties to achieve effective conversion and selectivity control.

Considering the above challenges, we herein report a ligand-free, dual-active-site heterogeneous Rh catalyst that features proximal Rh single atoms and nanoclusters co-anchored on nitrogen-doped carbon for the challenging hydroformylation of sterically hindered DIB. Systematic optimization of the calcination temperature yielded the Rh/N-AC-650 catalyst, which exhibits an optimized surface Rh^{3+} /Rh^{0} ratio together with a maximized pyridinic N content. This meticulously designed catalyst

Just Accepted

exhibits exceptional catalytic activity and excellent stability. Remarkably, it sustains steady-state performance for over 200 h under continuous-flow conditions, while maintaining structural integrity without significant metal leaching. It is also applicable for the hydroformylation of a wide range of olefins, demonstrating broad substrate generality. Comprehensive characterizations combined with theoretical calculations reveal that electronic interactions between the proximal Rh single atoms and nanoclusters impart a synergistic effect. This dual-active-site structure facilitates H_2 dissociation to generate key Rh-hydride species, strengthens DIB adsorption while simultaneously moderating CO chemisorption. This synergy also drastically lowers the energy barrier for the rate-determining CO insertion step, thereby substantially boosting the overall catalytic activity. Furthermore, pyridinic N speces in the carbon support are crucial in stabilizing the Rh species against aggregation and leaching, accounting for high stability. This work establishes a new framework for the rational design of high-performance and ligand-free heterogeneous Rh catalysts for olefin hydroformylation.

2 Results and Discussion

2.1 Catalyst synthesis and characterization

Figure 1a illustrates the synthesis of a dual-active-site heterogeneous Rh catalyst with isolated Rh single atoms and nanoclusters co-anchored on nitrogen-doped carbon. The nitrogen-doped activated carbon support (denoted as N-AC) was prepared by pyrolyzing a physical mixture of activated carbon and urea under a nitrogen atmosphere at 500 ºC, achieving a maximum N content of up to 7.10 wt% (**Figure S1a**). N_2 adsorption–desorption measurements of the N-AC support (Figure S1b) reveal a high specific surface area of 1336.5 $m^2 \cdot g^{-1}$ and an average pore size of 4.55 nm, providing an ideal platform for the dispersion of Rh active sites and efficient mass transport during the reaction. Subsequently, Rh species were immobilized onto the N-AC support through a conventional incipient wetness impregnation method followed by calcination at specified temperatures under a nitrogen atmosphere. The resulting materials

Just Accepted

were designated as Rh/N-AC-T, where T represents the calcination temperature (T = 550, 650, 750, and 850°C, respectively), while the sample without calcination treatment was denoted as Rh/N-AC. Inductively coupled plasma optical emission spectroscopy (ICP-OES) measurements reveal that the as-prepared catalysts had nearly identical Rh loadings regardless of the calcination temperatures, namely 0.43 wt% for Rh/N-AC, 0.42 wt% for Rh/N-AC-550, 0.41 wt% for Rh/N-AC-650, 0.40 wt% for Rh/N-AC-750, and 0.40 wt% for Rh/N-AC-850, respectively (**Table S1**), ensuring that performance variations are attributable to structural differences rather than metal content.

The morphology and dispersion of the Rh species were scrutinized using high-resolution transmission electron microscopy (HR-TEM), high-angle annular dark field-scanning transmission electron microscopy (HAADF-STEM), and X-ray diffraction (XRD). HR-TEM and aberration-corrected (AC) HAADF-STEM images of Rh/N-AC (**Figure 1b** and **Figure 1g**) confirm the exclusive formation of isolated Rh single atoms uniformly distributed across the support. In contrast, the Rh/N-AC-T samples exhibit a temperature-dependent evolution of Rh aggregates (**Figure 1c-f**). The average aggregate sizes increased from 0.92 nm at 550°C to 3.87 nm at 850°C, indicating that higher calcination temperatures facilitate the aggregation of isolated Rh single atoms into Rh nanoclusters (<2 nm) or larger, highly crystalline nanoparticles. This was further evidenced by the observation of well-resolved lattice fringes with an interplanar *d*-spacing of 0.190 nm (**Figure S2a-b**), corresponding to the (200) crystal plane of face-centered cubic (fcc) metallic Rh. Notably, AC HAADF-STEM images (**Figure 1g-k**) demonstrate the coexistence of Rh single atoms (marked with dashed circles) and nanoclusters or nanoparticles (marked with solid circles) in catalysts, depending on the calcination temperature. Moreover, as the calcination temperature increased, the population of isolated Rh single atoms gradually decreased, while Rh aggregates became predominant, in particular, almost no isolated Rh single atoms remained in Rh/N-AC-850. This further confirms the high-temperature-driven aggregation of Rh single atoms, consistent

Just Accepted

with the HR-TEM observations. The intensity profile analysis and 3D atom-overlapping Gaussian-function fitting mapping (**Figure 1l-p**) further verify this dual-site architecture. Energy-dispersive X-ray (EDX) elemental mapping (Figure S2c-d) of Rh/N-AC-650 further confirms the simultaneous presence of Rh single atoms and nanoclusters. XRD patterns (**Figure S3a**) show only broad diffraction peaks at approximately 22° and 44°, corresponding to the characteristic (002) and (100) planes of the graphitic carbon support, respectively, for the samples calcined below 750°C, indicating the high dispersion and low crystallinity of Rh species. In contrast, Rh/N-AC-850 exhibits a distinct metallic Rh (220) diffraction peak at 68.2°, consistent with the formation of larger nanoparticles.

Just Accepted

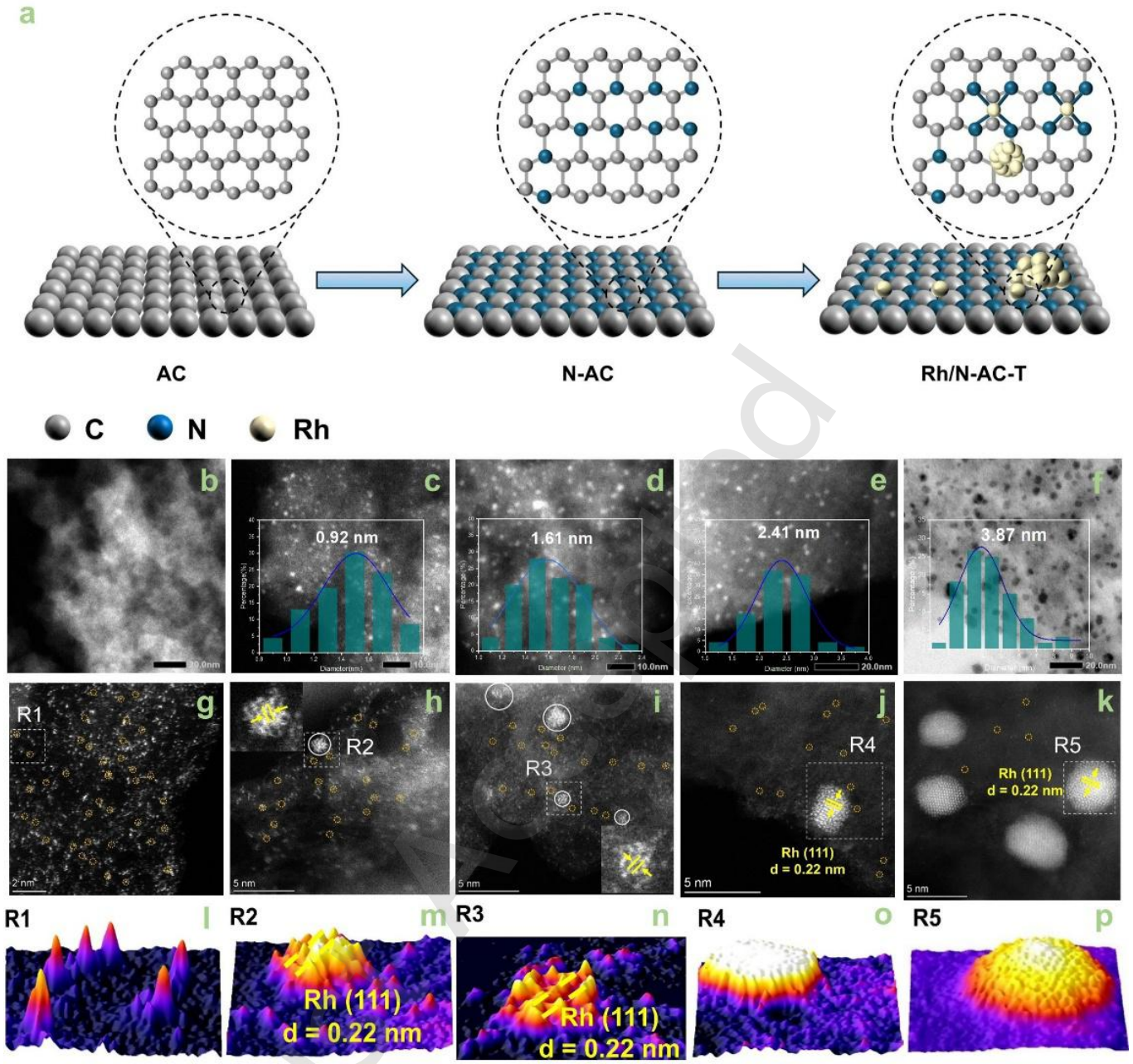


Figure 1. Synthesis, morphological and structural characterization of the Rh/N-AC-T catalysts. (a) Schematic representation of the multi-step synthesis of the Rh/N-AC-T catalysts. (b–f) HAADF-STEM images and corresponding Rh particle size distributions of (b) Rh/N-AC, (c) Rh/N-AC-550, (d) Rh/N-AC-650, (e) Rh/N-AC-750, and (f) Rh/N-AC-850. (g–k) AC-HAADF-STEM images of (g) Rh/N-AC, (h) Rh/N-AC-550, (i) Rh/N-AC-650, (j) Rh/N-AC-750, and (k) Rh/N-AC-850. Rh single atoms (SAs) and ultrasmall Rh clusters are indicated by dashed and solid circles, respectively. (l–p) Three-dimensional atom-overlapping Gaussian-function fitting maps of Regions 1–5 (R1–R5) in Figure 1g–k.

X-ray photoelectron spectroscopy (XPS) was performed to probe the surface composition and chemical state of the Rh/N-AC and Rh/N-AC-T catalysts. The XPS survey spectrum (**Figure S3b**) confirms the presence of C, N, O, and Rh elements in all catalysts, indicating successful nitrogen doping and dispersion of Rh species on the carbon. The high-resolution C 1s XPS spectrum (**Figure S3c**) was

deconvoluted into four peaks at 284.6, 285.1, 286.2, and 288.5 eV, corresponding to C-C, C-N, C-O, and O-C=O bonds, [36] respectively. The N 1s XPS spectrum (**Figure 2a**) was fitted with five distinct peaks at binding energies of 398.6, 399.8, 400.3, 401.1, and 402.7 eV, attributed to pyridinic N, Rh-N species, pyrrolic N, graphitic N, and oxidized N species, respectively. [37] The presence of Rh–N species provides compelling evidence for the coordination of Rh with nitrogen species in the carbon support. The relative intensity of the Rh-N peak gradually decreases with increasing calcination temperature from 550 to 850°C, reflecting a reduced population of Rh single atoms on the surface, as observed in AC HAADF-STEM. The high-resolution Rh 3d XPS spectra of Rh/N-AC-T (**Figure 2b**) display four characteristic peaks, corresponding to metallic Rh^0 species (Rh $3d_{5/2}$ at 307.7 eV and Rh $3d_{3/2}$ at 312.4 eV) [38] and oxidized Rh^{3+} species (Rh $3d_{5/2}$ at 309.9 eV and Rh $3d_{3/2}$ at 314.6 eV) [39], indicating the presence of Rh^0 and Rh^{3+} species on the catalyst surface. In Rh/N-AC, only Rh^{3+} species were detected, confirming the atomic dispersion of Rh species. As the calcination temperature rises, the Rh^0 signal strengthens at the expense of Rh^{3+}, signifying the high-temperature-driven aggregation of Rh single atoms into metallic aggregates, consistent with the TEM, HAADF-STEM, and XRD results. Quantitative analysis based on XPS reveals that the surface Rh^{3+}/Rh^0 ratio decreases from 2.54 in Rh/N-AC-550 to 1.17 in Rh/N-AC-650, 0.72 in Rh/N-AC-750, and 0.41 in Rh/N-AC-850, respectively, as summarized in **Figure 3e**. It should be noted that these XPS-derived Rh^{3+} /Rh^0 ratios describe the relative near-surface Rh species distribution and should not be directly interpreted as quantitative single-atom-to-cluster population ratios.

X-ray absorption spectroscopy (XAS) measurements were conducted to further elucidate the chemical state and local coordination environment of Rh species in the catalysts. The normalized Rh K-edge X-ray absorption near-edge structure (XANES) spectra of the catalysts (**Figure 2c**) were compared with those of Rh foil and Rh_2O_3 references. The absorption edges of all catalysts lie between those of Rh foil and Rh_2O_3, indicating that the average oxidation states of the Rh species are between 0 and +3. With

Just Accepted

increasing calcination temperature, both the absorption edge and white-line intensity progressively shift toward those of Rh foil, indicating progressive reduction of Rh^{3+} species. Fourier-transformed (FT) k^2-weighted extended X-ray absorption fine structure (FT-EXAFS) curves in R space of Rh/N-AC-T (**Figure 2d**) exhibit two prominent peaks at approximately 1.48 Å and 2.38 Å, attributed to Rh-N and Rh-Rh scattering paths, respectively, confirming the coexistence of atomically dispersed Rh sites and aggregates. In Rh/N-AC, the absence of Rh-Rh coordination scattering verifies the presence of exclusive Rh single atoms. Of note, the intensity of the Rh-Rh peak increases with rising calcination temperatures, indicating a shift toward larger Rh aggregates. The slight deviation of the Rh-Rh peak position for Rh/N-AC-550 relative to Rh foil can be attributed to the ultrasmall size of the Rh nanoclusters with low crystallinity, [40] as supported by HR-TEM observations and previous studies. The wavelet transform (WT) EXAFS contour plots (**Figure 2f**) further distinguish the backscattering atoms in both R and k spaces. A maximum intensity at ~5 $Å^{-1}$ is assigned to Rh-N coordination, while a secondary maximum intensity at ~7.5 $Å^{-1}$ corresponds to the Rh-Rh coordination. [41] Consistent with the FT-EXAFS results, the intensity for the Rh-Rh feature strengthens with increasing calcination temperature. The average coordination number (CN) was derived from the quantitative least-squares EXAFS fitting in the R space (**Figure 2e**, **Figure S4** and **Table S2**). The average of the Rh-N coordination number (CN) for the calcined Rh/N-AC-T catalysts was consistently refined to approximately 4 at a bond distance of 2.03 ± 0.01 Å, indicating a stable Rh-N_4 configuration. Concurrently, the CN of the Rh-Rh scattering path (at a bond distance of 2.68 ± 0.02 Å) shows a progressive increase with calcination temperature from 1.75 for Rh/N-AC-550 to 2.75 for Rh/N-AC-650, to 4.25 for Rh/N-AC-750, and further to 6.0 for Rh/N-AC-850. These results again suggest a gradual transition from atomically dispersed Rh sites to metallic aggregates as the calcination temperature rises, corroborating the HR-TEM, AC HAADF-STEM, and XPS observations.

Just Accepted

To further verify the dispersion state of Rh species in the Rh/N-AC-T catalysts, in situ diffuse reflectance infrared Fourier transform spectroscopy (DRIFTS) with CO as the probe molecule was performed. The absorption bands observed at around 2170 and 2118 cm^{-1} correspond to gaseous CO molecules, [42] which gradually disappear after the purging process due to the weak interaction with the catalyst surface (**Figure S5**). For Rh/N-AC, two distinct peaks centered at 2088 and 2016 cm^{-1} were clearly observed (**Figure 2g**), which are typically attributed to the symmetric and asymmetric stretching vibrations of *gem*-dicarbonyl species ($Rh(CO)_2^+$) adsorbed on positively charged Rh atoms. [43] Meanwhile, a small band at 2054 cm^{-1}, assignable to linearly chemisorbed CO on Rh [44], was observed in the absence of a bridged-CO band in the 1900–1800 cm^{-1} region. This confirms the atomic dispersion of Rh species, consistent with the characterization results described above. For Rh/N-AC-550 and Rh/N-AC-650, in addition to the *gem*-dicarbonyl species ($Rh(CO)_2^+$), a relatively weak peak at around 1834 cm^{-1} appears, which can be attributed to bridged CO on metallic Rh nanoclusters. [45] This observation is consistent with the coexistence of Rh single atoms and nanoclusters. Notably, the *gem*-dicarbonyl species ($Rh(CO)_2^+$) doublet redshifted as the cluster size increases: from 2088 and 2016 cm^{-1} in Rh/N-AC to 2082 and 2008 cm^{-1} in Rh/N-AC-550, and to 2077 and 2002 cm^{-1} in Rh/N-AC-650, respectively, indicating increased electron density at the isolated Rh sites. [43] This suggests a significant electronic interaction between the proximal Rh single atoms and nanoclusters. In contrast, for Rh/N-AC-750 and Rh/N-AC-850, the gem-dicarbonyl bands disappear, whereas the bridged-CO band becomes dominant, indicating nanoparticle-dominated Rh surfaces, consistent with the HR-TEM, XPS, and XAS results.

Just Accepted

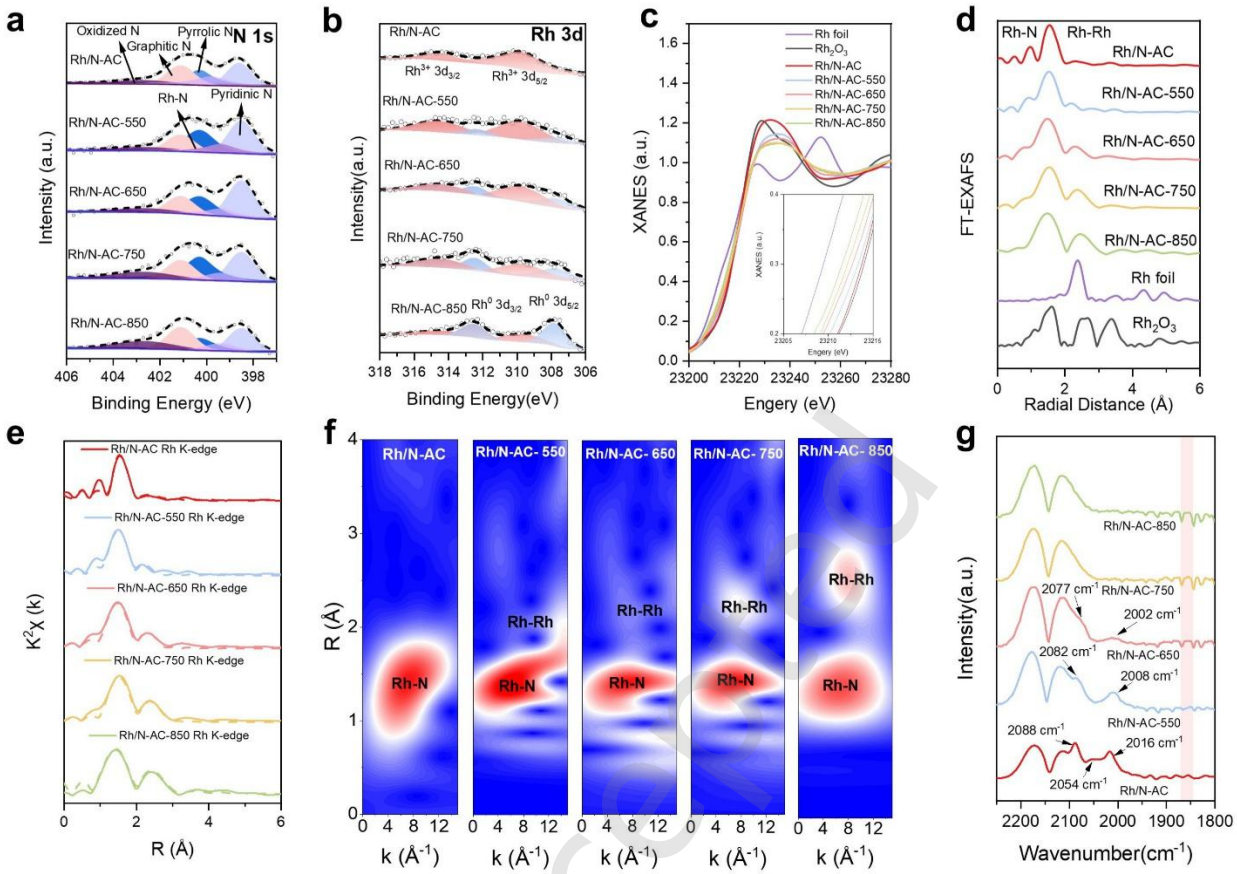


Figure 2. Spectroscopic and electronic structure characterization of the Rh/N-AC-T catalysts. (a) High-resolution N 1s XPS spectra of Rh/N-AC-T catalysts prepared at different calcination temperatures. (b) High-resolution Rh 3d XPS spectra. (c) Rh K-edge XANES spectra for Rh/N-AC-T, benchmarked against Rh foil and Rh_2O_3 references. The inset provides a magnified view of the absorption edge. (d) Corresponding k^3-weighted, Fourier-transformed (FT) Rh K-edge EXAFS spectra in R-space. (e) R-space EXAFS fitting curves (dashed lines) overlaid on the experimental data (solid lines) for Rh/N-AC-T. (f) WT of Rh K-edge EXAFS oscillations for Rh/N-AC-T and Rh/N-AC. (g) In situ CO-DRIFTS spectra of the Rh/N-AC-T catalysts recorded at room temperature after CO adsorption and subsequent N_2 purging for 10 min.

2.2 Catalytic performance in DIB hydroformylation

The catalytic activities of the as-synthesized Rh/N-AC and Rh/N-AC-T catalysts were evaluated for the hydroformylation of DIB, a sterically hindered olefin. The reactions were conducted in toluene at 120°C under 6 MPa pressure of syngas (H_2/CO, v/v = 1/1) for 6 h. As illustrated in **Figure 3a**, the catalytic activity follows a volcano-shaped dependence on the calcination temperature, with Rh/N-AC-650 exhibiting the highest activity among all catalysts tested. Notably, despite being composed exclusively of Rh single atoms with theoretically maximized metal atom utilization, Rh/N-AC did not yield the highest catalytic activity. Its activity was lower than those of Rh/N-AC-550 and Rh/N-AC-650, although it

JUST ACCEPTED

remained superior to that of Rh/N-AC-750 and Rh/N-AC-850, where Rh nanoparticles were predominantly formed. The inferior activity of the latter two catalysts can be attributed to the lower surface-to-volume ratio of the larger Rh nanoparticles. These results suggest that the coexistence of atomically dispersed Rh species and Rh nanoclusters provides a more favorable catalytic configuration for DIB hydroformylation than either isolated Rh atoms or nanoparticles alone. This finding is consistent with previous reports demonstrating that the synergistic interactions between single metal atoms and metal clusters/nanoparticles can boost catalytic performance.[46,47] To further elucidate the synergistic effect between Rh single atoms and nanoclusters, a physical mixture of Rh/N-AC and Rh/N-AC-700 was employed as a control catalyst for the reaction. Despite containing comparable Rh species, the physically mixed catalyst exhibited significantly lower activity than Rh/N-AC-650 under identical reaction conditions (**Figure S9**), highlighting the critical role of their integrated spatial arrangement within a single catalyst framework. This observation indicates that intimate coupling between Rh single atoms and nanoclusters, rather than their simple coexistence, is essential for achieving enhanced catalytic activity. Meanwhile, all catalysts maintained excellent selectivity toward the highly branched 3,5,5-trimethylhexanal (INA), exceeding 97% with only trace amounts of the hydrogenation byproducts, including diisobutane and 3,5,5-trimethylhexanol.

Given the high surface energy of sub-nanometer metal species, their structural stability under reaction conditions is a critical challenge. To assess this, parallel recycling experiments were conducted. Each catalyst was carefully recovered after each run and then reused in the subsequent cycle. Impressively, in addition to its outstanding activity, Rh/N-AC-650 demonstrated exceptional stability (**Figure 3b** and **Figure S6**), maintaining its activity over four consecutive cycles with only a slight decline under both high- and low-conversion conditions, primarily due to unavoidable physical mass loss during catalyst recovery rather than intrinsic deactivation. Both Rh/N-AC and Rh/N-AC-550 showed intermediate

Just Accepted

stability, with a gradual decline throughout the recycling tests. In stark contrast, both Rh/N-AC-750 and Rh/N-AC-850, which are dominated by Rh nanoparticles, suffered rapid deactivation, approaching complete loss of activity by the fourth run, underpinning their poor stability. To further evaluate the industrial potential of Rh/N-AC-650, we performed a long-term stability test in a continuous-flow fixed-bed reactor. Remarkably, it maintained a steady DIB conversion of approximately 80% and consistent INA selectivity over 200 h on-stream without significant fluctuation (**Figure 3c**), underscoring its potential for practical applications.

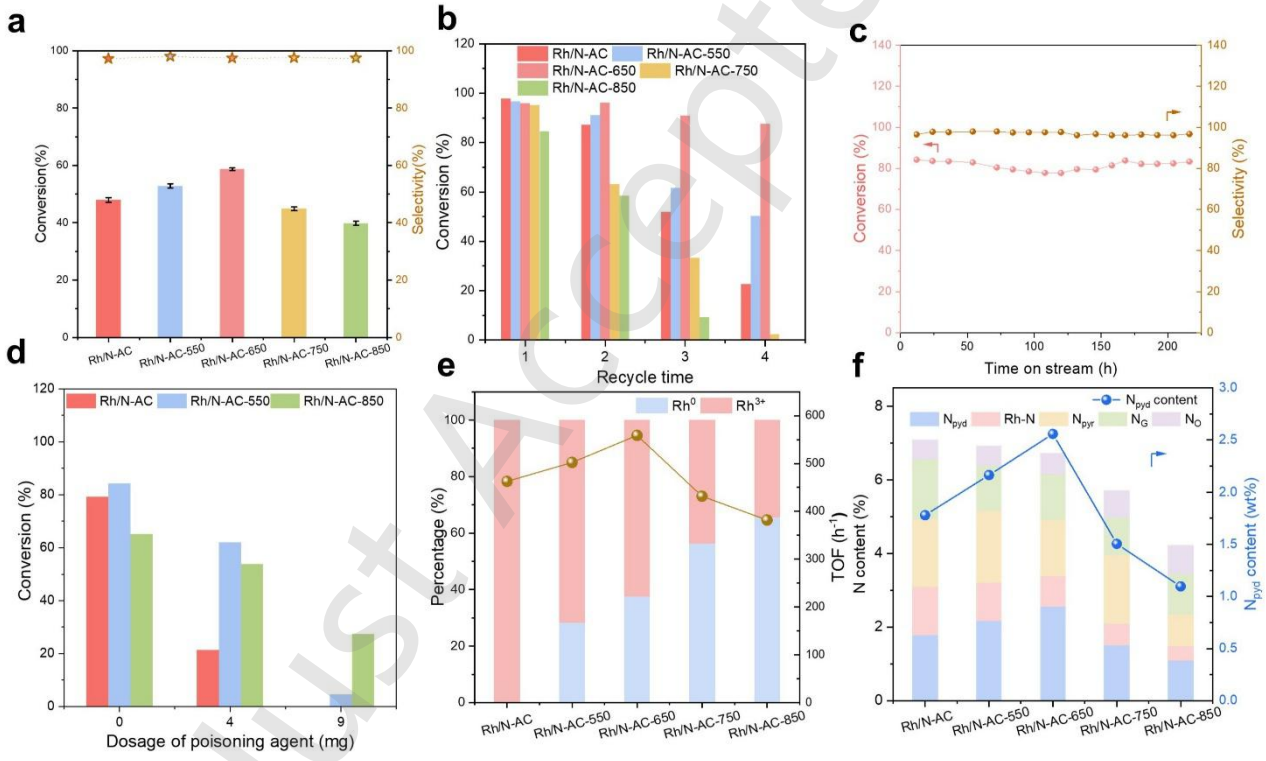


Figure 3. Catalytic performance in the hydroformylation of DIB. (a) DIB conversion and aldehyde selectivity over Rh/N-AC-T catalysts as a function of calcination temperature. Batch reaction conditions: 120 °C, 6 MPa syngas (CO/H_2 = 1:1, v/v), 6 h. (b) Recycling performance of Rh/N-AC, Rh/N-AC-550, Rh/N-AC-650, Rh/N-AC-750, and Rh/N-AC-850 over four consecutive runs. (c) Long-term stability test (216 h) of Rh/N-AC-650 in a fixed-bed reactor at 120 °C and 6 MPa syngas, with a DIB/toluene volume ratio of 1:4, a liquid flow rate of 0.3 $mL \cdot h^{-1}$, and a syngas flow rate of 10 $mL \cdot min^{-1}$. (d) Effect of KSCN dosage on DIB conversion over Rh/N-AC, Rh/N-AC-550, and Rh/N-AC-850. (e) XPS-derived relative proportions of surface Rh^0 and Rh^{3+} species and the corresponding TOF values as a function of calcination temperature. (f) Relative contents of pyridinic N, pyrrolic N, graphitic N, and oxidized N derived from N 1s XPS.

In addition to DIB hydroformylation, the scope of olefin substrate was also examined over the Rh/N-AC-650 catalyst. As summarized in **Table S3**, the catalyst exhibited broad applicability across a range of

Just Accepted

olefins, including α-olefins with different chain lengths, cyclic olefins, and aromatic olefins, affording the corresponding aldehydes with high activity and selectivity. To benchmark its catalytic performance against state-of-the-art heterogeneous Rh catalysts, 1-hexene hydroformylation was selected as a model reaction, as systematic comparison for DIB hydroformylation remain scarce due to the limited availability of reported data. As shown in Figure S10, after taking key parameters, including reaction temperature and syngas pressure into account, Rh/N-AC-650 exhibited a competitive turnover frequency (TOF) compared with previously reported heterogeneous Rh catalysts, highlighting its high catalytic efficiency for olefin hydroformylation. Note that, because the reported studies employ different olefin substrates, reactor configurations, reaction conditions, conversion levels, and TOF normalization methods, direct comparison of the reported TOFs should be made with caution and does not be necessarily reflect differences in intrinsic site activity.

2.3 Structure-performance relationships

To elucidate the distinct roles of Rh single atoms and nanoclusters/nanoparticles in DIB hydroformylation, poisoning experiments were performed using KSCN, a well-established selective probe for atomically dispersed metal sites. [48] As shown in **Figure 3d**, the addition of 1.0 equiv. (4 mg) of KSCN into the reaction catalyzed by Rh/N-AC led to a drastic suppression of catalytic activity, decreasing DIB conversion from 80% to 21%. Upon increasing the KSCN amount to 9 mg, the catalytic activity was completely inhibited. In comparison, Rh/N-AC-550 also exhibited decreased activity after KSCN addition; however, the extent of inhibition was significantly smaller than that observed for Rh/N-AC under identical conditions. For Rh/N-AC-850, the influence of KSCN poisoning was further diminished, despite its intrinsically lower catalytic activity. Given the nearly identical Rh content across all samples (**Table S1**), these results indicate that both Rh single atoms and aggregated Rh species, including nanoclusters and nanoparticles, participate in the hydroformylation catalytic cycle. To compare

Just Accepted

the CO adsorption capacities of the catalysts, CO pulse chemisorption measurements were performed across the catalyst series (**Figures S7** and **S8**). Among all catalysts, Rh/N-AC-650 exhibited the highest CO uptake, suggesting a relatively high population of CO-accessible Rh species. However, given the potentially different CO/Rh adsorption stoichiometries associated with distinct Rh nuclearities and coordination environments, the measured CO uptake is considered a relative descriptor rather than a quantitative measure of the accessible Rh active site population. More importantly, the catalytic activity shows an apparent correlation with the XPS-derived surface Rh^{3+} /Rh^{0} ratio, with Rh/N-AC-650 exhibiting the highest TOF at a ratio of 1.17 (Figure 3e). Note that, this ratio serves as an empirical descriptor of the surface Rh oxidation-state distribution rather than a direct measure of the relative populations of Rh single atoms and nanoclusters. The observed correlation suggests that an appropriate balance of surface Rh electronic states is beneficial for catalytic activity.

We next sought to elucidate the underlying reasons for the remarkable stability of Rh/N-AC-650. The structural robustness of the catalysts after hydroformylation was evaluated by postreaction characterization. As shown in Figure S11, Rh K-edge XANES, R-space FT-EXAFS, HR-TEM, AC-HAADF-STEM, and XPS analyses revealed that the spent Rh/N-AC-650 catalyst retained essentially the same Rh K-edge position, local coordination environment, average particle size, and oxidation state as the fresh catalyst. Importantly, HAADF-STEM analysis of the Rh/N-AC-650 catalyst recovered after the long-term fixed-bed reaction (**Figure S11g**) revealed only a slight change in the Rh particle-size distribution, indicating that Rh aggregation was effectively suppressed during prolonged continuous-flow operation. These results demonstrate that the Rh single-atom/nanocluster architecture remains largely intact during catalysis, highlighting the exceptional structural stability of Rh/N-AC-650 under hydroformylation conditions. To exclude the possibility of homogeneous catalysis by dissolved Rh species, a hot-filtration experiment was further performed (Figure S11c). After removal of the solid

Just Accepted

catalyst, the filtrate showed negligible additional conversion under identical conditions, indicating no leaching of Rh species into the reaction medium. In sharp contrast, the spent Rh/N-AC, Rh/N-AC-550, Rh/N-AC-750, and Rh/N-AC-850 catalysts all exhibited increased Rh aggregation after four recycling runs (**Figure S12**), indicating their inferior structural stability relative to Rh/N-AC-650 under the reaction conditions. Consistently, ICP-OES analysis detected negligible Rh loss from Rh/N-AC-650, whereas appreciable metal loss was observed for Rh/N-AC-850 (**Table S4**). Collectively, these results demonstrate that Rh/N-AC-650 effectively suppresses both Rh aggregation and metal leaching during hydroformylation.

To further examine the factors associated with the enhanced stability of Rh/N-AC-650, we analyzed the evolution of nitrogen species in the carbon support. Pyridinic N (symbolled as N_{pyd}) is well known to strongly anchor transition-metal species on nitrogen-doped carbon supports, thereby strengthening metal-support interactions and suppressing metal migration, coalescence, and Ostwald ripening. [49] Although the total N content steadily declined with increasing calcination temperature, that is, from 7.10 wt% in Rh/N-AC to 6.94 wt% in Rh/N-AC-550, to 6.63 wt% in Rh/N-AC-650, to 5.72 wt% in Rh/N-AC-750, and to 4.23 wt% in Rh/N-AC-850 (**Table S1**), the relative fraction of pyridinic N, as determined by N 1s XPS, exhibited a volcano-shaped dependence on calcination temperature (**Figure 3f**), reaching a maximum for Rh/N-AC-650. Notably, the variation in pyridinic N content aligns closely with the trends in catalytic activity and recyclability. These findings identify pyridinic N as the key anchoring site that stabilizes the Rh single-atom and nanocluster ensemble by strengthening metal-support interactions and suppressing Rh migration and leaching, thereby providing a structural basis for the superior activity and high stability of Rh/N-AC-650.

To gain further molecular-level insights into the DIB hydroformylation reaction and its correlation with the distinct catalytic performances of the Rh/N-AC and Rh/N-AC-T catalysts, density functional theory

Just Accepted

(DFT) calculations were performed. Based on the characterization results, three representative models were constructed: an isolated Rh single-atom model (Rhs) to represent Rh/N-AC, a coupled Rh single-atom–nanocluster model (Rhs–Rhc) to represent Rh/N-AC-650, and a Rh nanoparticle model (Rhn) to represent Rh/N-AC-850. Charge density difference maps and electron localization function (ELF) analysis (**Figures S13** and **S14**) indicate electronic redistribution between the Rh single-atom and nanocluster within the representative Rhs-Rhc model, which is qualitatively consistent with the changes in the Rh electronic environment inferred from the experimental characterization. Such an intimate dual-site configuration enables a large fraction of Rh atoms to interact directly with nitrogen dopants, thereby reinforcing metal-support interactions and improving structural robustness. In contrast, for larger Rh nanoparticles, only the interfacial Rh atoms are effectively anchored by the support, whereas surface-exposed Rh atoms remain susceptible to leaching and aggregation under hydroformylation conditions.

Projected density of states (PDOS) and Bader charge analysis (**Figures S15** and **Table S5**) further reveal substantial electronic-structure modulation arising from the interaction between Rh single atoms and nanoclusters in the Rhs-Rhc configuration. Specifically, the d-band center of the Rhs shifts toward the Fermi level from -1.170 eV for isolated Rhs to -1.001 eV in the Rhs-Rhc configuration, whereas that of Rhc shifts upward from -1.243 eV in Rhn to -0.925 eV. These shifts indicate pronounced redistribution of the Rh electronic states upon formation of the Rhs-Rhc configuration. As illustrated in **Figure 4a** and **4b**, the Rhs-Rhc model provides favorable H_2 adsorption/activation while maintaining a moderate CO adsorption strength. In contrast, **Figure 4c** shows that DIB adsorption on the Rhs site becomes weaker upon incorporation of Rhs into the Rhs-Rhc configuration. Importantly, the weakened DIB adsorption should not be interpreted solely in terms of the shift in the d-band center. Given the bulky and highly branched structure of DIB, its adsorption is also strongly influenced by the local coordination geometry and steric environment of the Rh site. As further illustrated by the adsorption configurations in **Figure 4d**,

Just Accepted

the neighboring Rh cluster modifies not only the electronic structure but also the local geometric environment of Rhs, thereby altering the interaction between the C=C moiety of DIB and the isolated Rh center. Consequently, DIB adsorption on Rhs becomes less favorable in the Rhs-Rhc configuration, whereas the adjacent Rhc sites provide additional favorable adsorption configurations for DIB. Thus, rather than uniformly strengthening DIB adsorption at both Rh sites, the Rhs-Rhc configuration redistributes the adsorption preference of DIB between the isolated Rh and Rh-cluster sites.

As previously reported, CO chemisorption on catalytically active Rh sites plays a critical role in determining both catalytic activity and stability in heterogeneous Rh catalysis. [50] Recent molecular-level investigations of CO adsorption on Rh-based nanocatalysts have further demonstrated that CO adsorption behavior is sensitive to the size and local structural configuration of Rh ensembles, highlighting the critical influence of Rh nanostructure on CO accessibility and adsorption interactions.[51] In line with the Sabatier principle, an appropriate CO binding strength is essential to balance CO activation and site availability, as excessively strong CO adsorption can induce active-site blocking or promote the formation of soluble $Rh^{+}(CO)_n$ species, leading to catalyst deactivation and metal leaching. [52] In comparison, the Rhn model exhibits the strongest calculated CO adsorption energy (-1.19 eV), which may result in excessive CO coverage and facilitate the generation of leachable $Rh^{+}(CO)_n$ species. [53] This calculated trend is consistent with the experimentally observed greater tendency of Rh/N-AC-850 toward Rh leaching and aggregation during catalysis. Furthermore, the Rhs-Rhc configuration substantially lowers the activation energy barrier for H_2 dissociation, the key elementary step for generating Rh-hydride species (**Figure S16**), to 0.59 eV, which is markedly lower than those calculated for isolated Rhs (1.19 eV) or Rhn (0.91 eV). These results demonstrate that the synergistic electronic interaction between Rh single atoms and nanoclusters facilitates H_2 activation while regulating CO adsorption, thereby providing a molecular-level explanation for the improved catalytic activity and stability of Rh/N-AC-650

Just Accepted

in DIB hydroformylation.

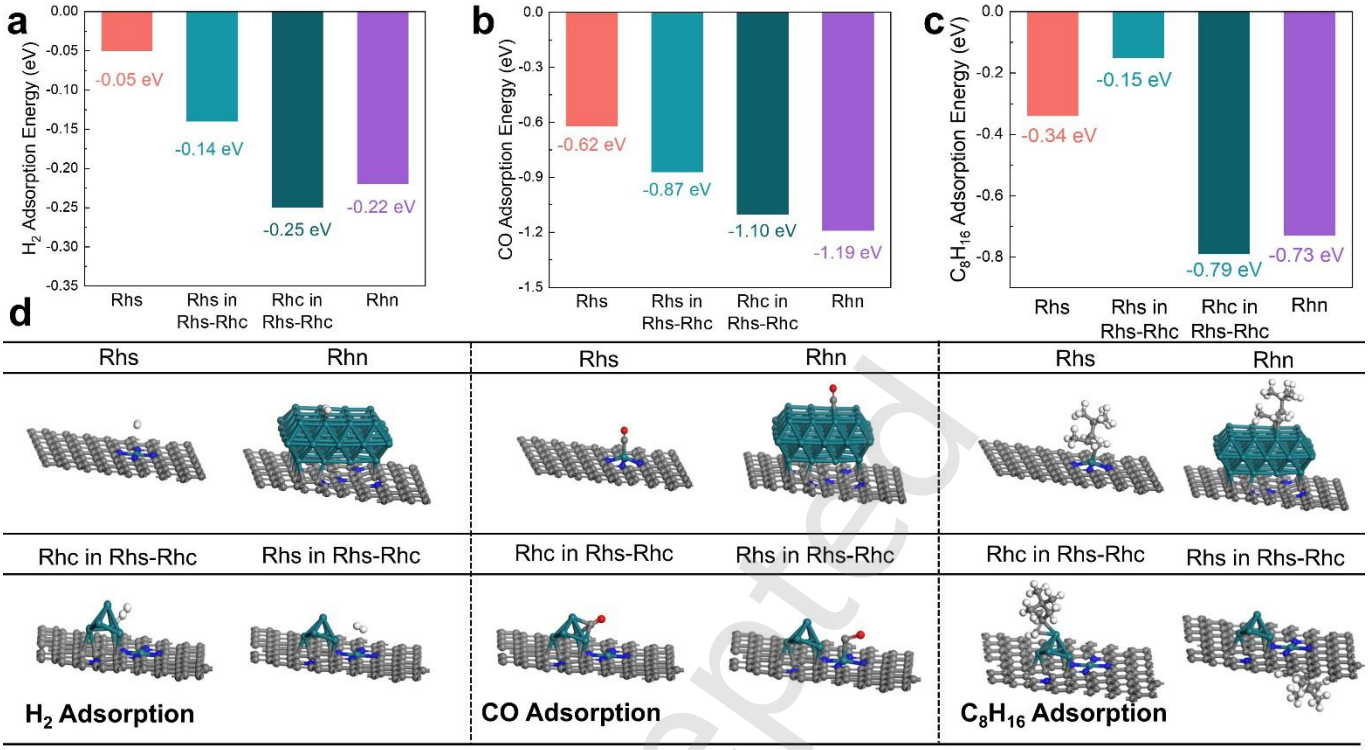
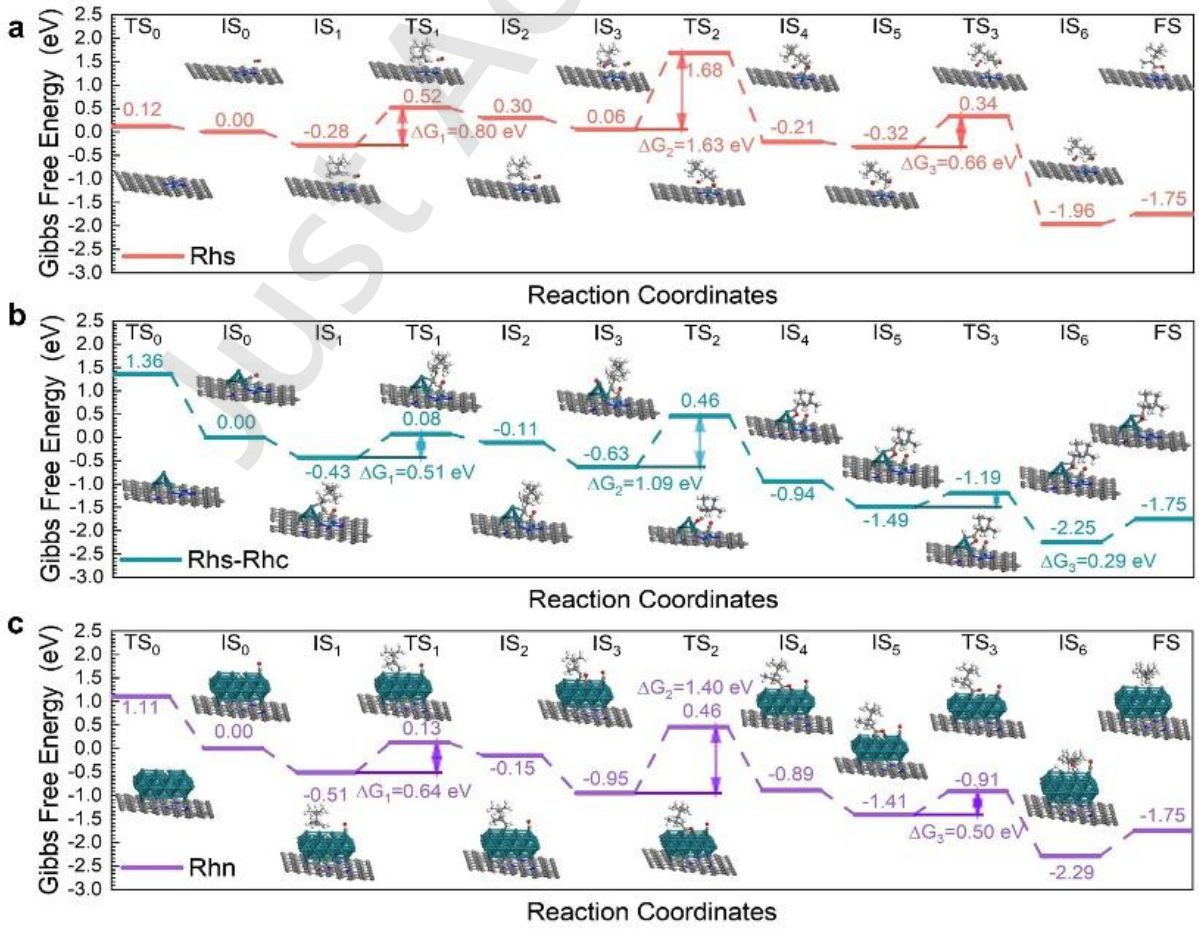


Figure 4. Adsorption energies of (a) H_2, (b) CO, and (c) DIB (C_8H_{16}) at different sites in the Rhs, Rhs–Rhc, and Rhn models. (d) Corresponding adsorption configurations of H_2, CO, and C_8H_{16} at different Rh sites in the Rhs, Rhs–Rhc, and Rhn models.



Just Accepted

Figure 5. Reaction pathways and the corresponding free-energy profiles for the Rhs, Rhs–Rhc, and Rhn models in DIB hydroformylation.

Finally, the Gibbs free-energy profiles for DIB hydroformylation were calculated to provide insight into the reaction pathway and the possible origin of the different catalytic behaviors of the representative Rh models. As shown in **Figure 5a-c**, the reaction proceeds through three key elementary steps involving three transition states: the first H insertion to generate the Rh-alkyl intermediate (TS1), CO insertion to form the Rh-acyl intermediate (TS2), and the second H insertion to generate INA (TS3). Among the elementary steps examined, CO insertion exhibits the highest calculated free-energy barrier for all three models (Rhs, Rhs-Rhc, and Rhn), suggesting that it is the rate-determining step within the adopted reaction pathways. Notably, the calculated CO-insertion barrier for the Rhs-Rhc configuration (1.09 eV) is lower than those for Rhs (1.63 eV) and Rhn (1.40 eV). This relative trend suggests that the coexistence of Rh single atoms and nanoclusters may facilitate CO insertion through a synergistic effect. Although the simplified structural models and the omission of solvent effects may affect the absolute energetic values, the relative barrier trend provides qualitative mechanistic insight into the potential role of the dual-site configuration and is consistent with the experimentally observed enhanced catalytic activity of Rh/N-AC-650.

3 Conclusion

In summary, we have developed a high-performance, ligand-free heterogeneous Rh catalyst featuring proximal dual active sites composed of Rh single atoms and nanoclusters coanchored on nitrogen-doped carbon. The optimized Rh/N-AC-650 catalyst exhibits exceptional catalytic activity for the challenging hydroformylation of sterically hindered DIB, surpassing both isolated single-atom and nanoparticle counterparts. Notably, it demonstrates remarkable structural stability and resistance to Rh leaching, enabling stable continuous-flow operation for over 200 h in a fixed-bed reactor. The superior performance stems from a synergistic interplay between adjacent Rh single atoms and nanoclusters.

Just Accepted

Combined experimental investigations and DFT calculations suggest that the intimate coupling between these two Rh species modulates the electronic structure and adsorption behavior of H_2 , CO, and DIB. In particular, the electronically modulated dual-site interface promotes H_2 activation and lowers the energy barrier of the rate-determining CO insertion step, thereby accelerating catalytic performance. Meanwhile, pyridinic N contributes to the stabilization of Rh species by strengthening Rh–support interactions and suppressing Rh migration, aggregation, and leaching under demanding reaction conditions. This work establishes proximal single atom–nanocluster dual sites as an effective catalyst design paradigm that integrates the advantages of atomic dispersion, cooperative activation, and structural durability. Beyond hydroformylation, this strategy provides a versatile platform for constructing multifunctional heterogeneous catalysts for challenging carbonylation reactions and other complex molecular transformations.

4 Methods

4.1 Catalyst Synthesis

4.1.1 Materials

Unless otherwise stated, all reagents and solvents were of analytical grade and used as received without further purification. $RhCl_3 \cdot 3H_2O$ (99.95% metal basis) and urea were purchased commercially from Sigma-Aldrich. Activated carbon (200 mesh) was purchased from Shanghai Yien Chemical Technology Co., Ltd. Analytic grade toluene was purchased from Sino-Pharm Chemical Reagent Co., Ltd. Diisobutylene (DIB) was supplied by Shandong Chambroad Petrochemical Co., Ltd (Binzhou), China.

4.1.2 Catalyst synthesis

Nitrogen-doped activated carbon was first prepared as follows: urea (1.5 g) and activated carbon (0.3 g) were thoroughly ground in an agate mortar to obtain a homogeneous mixture. The resulting powder was then transferred to a tube furnace and heated to 500 °C at a ramp rate of 2 $°C \cdot min^{-1}$ under a continuous N_2 flow of 100 $mL \cdot min^{-1}$. After being maintained at 500 °C for 2 h, the sample was

Just Accepted

allowed to cool naturally to room temperature under the same inert atmosphere, yielding the nitrogen-doped carbon (labelled as N-AC). Subsequently, N-AC (1.5 g) was dispersed in 80 mL of isopropanol containing $RhCl_3 \cdot 3H_2O$ (0.001 g mL^{-1}, 2.5 mL) under stirring for 48 h at ambient temperature. The solid was then collected by centrifugation, washed three times with ethanol, and vacuum-dried at 60 °C for 12 h, which was labelled as Rh/N-AC. Finally, the dried powder was calcined in a tube furnace under a N_2 flow (100 mL·min^{-1}) for 4 h at 550, 650, 750 or 850 °C with a heating rate of 2 °C·min^{-1}. The resulting materials are denoted as Rh/N-AC-T, where T represents the calcination temperature.

4.1.3 General procedure for hydroformylation of DIB

Typically, to a 50 mL glass vessel with a stirring bar was added DIB (6.38 mmol), catalyst (40 mg), and toluene (10 mL). The glass vessel was then loaded into an autoclave. The autoclave was sealed and purged with CO/H_2 three times, and then pressurized with CO/H_2 (1/1, v/v) to 6 MPa and placed in a heating oven at the desired temperature and stirred at 400 rpm for the duration of the desired reaction time. After the reaction, the autoclave was allowed to cool down to room temperature, and the pressure was released slowly in a well-ventilated hood. The catalyst was separated from the reaction mixture by filtration, and the liquid was analyzed by GC and GC-MS to determine the reaction conversion and selectivity using n-dodecane as an external standard.

The substrate conversion, aldehyde selectivity, aldehyde yield, and turnover frequency (TOF) were calculated using the following equations. The amount of Rh used for TOF calculation was based on the actual Rh loading determined by ICP-OES.

$$Conversion\ (\%) = \frac{n_{DIB,0} - n_{DIB}}{n_{DIB,0}} \times 100\%$$

$$Selectivity\ (\%) = \frac{n_{aldehydes}}{n_{converted\ DIB}} \times 100\%$$

$$TOF = \frac{n_{\text{converted substrate}}}{n_{Rh} \times t}$$

$$\text{Product yield}\ (\%) = \frac{\text{conversion}\ (\%) \times \text{selectivity}\ (\%)}{100}$$

where $n_{DIB,0}$ and n_{DIB} represent the initial and remaining molar amounts of DIB, respectively; $n_{aldehydes}$ is

Just Accepted

the total molar amount of aldehyde products; n_{Rh} is the molar amount of Rh in the catalyst; and t is the reaction time (h).

4.1.4 General procedure of the stability test for Rh/N-AC-T in batch

Typically, to a 50 mL glass vessel with a stirring bar was added DIB (6.38 mmol), catalyst (40 mg), and toluene (10 mL). The glass vessel was then loaded into an autoclave. The autoclave was sealed and purged with CO/H_2 three times, and then pressurized with CO/H_2 (1/1, v/v) to 6 MPa and placed in a heating oven at the desired temperature and stirred at 400 rpm for the duration of the desired reaction time. After the reaction, the autoclave was cooled to room temperature, and the remaining gas was slowly released in a well-ventilated hood. The catalyst was centrifuged three times with methanol and then dried in a vacuum drying oven at 60 °C for 12 h. The recovered catalyst was then subjected to the next cycle following the same procedure under identical conditions.

4.1.5 General procedure of the stability test for Rh/N-AC-650 in fixed bed

Hydroformylation performance of the catalyst was evaluated in a quartz fixed-bed reactor with an inner diameter of 8 mm and length of 140 mm, operated at 120 °C and 6 MPa of syngas. A layer of quartz wool was placed below the catalyst bed to secure its position, and 1 g of the catalyst was loaded into the reactor, with quartz wool placed on top of the catalyst. A mixture of DIB and toluene in a volume ratio of 1:4 was pumped into the reactor at a liquid flow rate of 0.3 $mL \cdot h^{-1}$. The syngas pressure was maintained at 6 MPa with a gas flow rate of 10 mL/min. Liquid samples were taken every 12 h for GC and GC–MS analysis to determine the conversion and selectivity.

4.2 Characterization

Scanning electron microscopy (SEM) images were obtained using a ZEISS GeminiSEM360 operated at an accelerating voltage of 0.5 kV. Transmission electron microscopy (TEM) images were acquired using a Hitachi H-7600 operated at 200 kV, and high-resolution TEM (HRTEM) images were

Just Accepted

obtained using a JEOL JEM-F200 operated at 200 kV. High-angle annular dark-field scanning transmission electron microscopy (HAADF-STEM) images and corresponding energy dispersive X-ray (EDX) images were obtained on a Thermo Fisher Scientific Themis Z equipped with a probe corrector, with a guaranteed resolution of 80 pm and an accelerating voltage of 200 kV. All XPS binding energies were calibrated using the C 1s peak at 284.8 eV. A Shirley background was consistently applied to all high-resolution Rh 3d spectra before peak deconvolution. For comparison of the relative distributions of Rh oxidation states, the background-corrected Rh 3d spectra were normalized to the total integrated Rh 3d peak area. Inductively coupled plasma optical emission spectroscopy (ICP-OES) was conducted on a PerkinElmer Optima 5300 DV instrument. Gas chromatography (GC) was conducted on Shimazu Nexis GC-2030 equipped with FID detector and HP-5 capillary column. Gas chromatography-mass spectrometry (GC-MS) analysis was carried out on a Shimazu GCMS-QP2010 SE instrument equipped with HP-5 capillary column using helium carrier gas. XAFS measurements were carried out using a Si (311) double-crystal monochromator (NW10A, PFAR) at room temperature at the Institute of Materials Structure Sciences of High Energy Accelerator Research Organization (KEK). The monochromator energy was calibrated using a Pd foil. The XAFS data were analyzed using IFEFFIT. The XAFS raw data were background subtracted, normalized and Fourier transformed by standard procedure within the ATHENA program. The acquired EXAFS data were processed according to the standard procedures using the ATHENA module implemented in the IFEFFIT software packages. CO-DRIFTS measurements were performed on a Bruker Vertex 80V Fourier-transform infrared spectrometer equipped with an in situ diffuse-reflectance cell, an MCT detector, and ZnSe windows. Prior to CO adsorption, the catalyst was pretreated under flowing N_2 (15 mL·min^{-1}) at 120 °C for 60 min to remove weakly adsorbed surface species. The sample was then cooled to room temperature under flowing N_2. Subsequently, a CO/N_2 mixture (1:19, v/v) was introduced at a total flow rate of 15 mL·min^{-1}, and CO adsorption was

Just Accepted

conducted at room temperature for 60 min. After adsorption, the gas feed was switched to pure N_2 (15 $mL \cdot min^{-1}$) at room temperature to remove gas-phase and weakly adsorbed CO species. The CO-DRIFTS spectra used for comparison were collected after 10 min of N_2 purging at room temperature. Because the black N-doped activated-carbon support exhibits strong broadband infrared absorption and low diffuse reflectance, the signals from surface-adsorbed CO were relatively weak. Accordingly, a high-sensitivity MCT detector was employed to enhance the signal-to-noise ratio. Nitrogen adsorption–desorption data were obtained on a Micromeritics ASAP 2460 static volumetric sorption analyzer. The powder samples were outgassed for 12 h at 120 °C before the measurements. CO pulse chemisorption measurements were performed to evaluate the CO adsorption capacity of the Rh/N-AC-T catalysts. Typically, 100 mg of catalyst was pretreated in a flowing H_2/Ar mixture at 300 °C for 1 h. The sample was subsequently purged with high-purity He at the same temperature for 30 min to remove residual gases and weakly adsorbed species. After pretreatment, the catalyst was cooled to 50 °C under flowing He and maintained at this temperature until a stable detector baseline was obtained. Pulses of 10 vol% CO/He were then sequentially introduced into the system until adsorption saturation was reached, as indicated by unchanged peak areas for consecutive CO pulses. The total amount of chemisorbed CO was determined from the cumulative difference between the injected and detected CO pulse areas. Because the Rh/N-AC-T catalysts contain Rh species with different nuclearities and coordination environments, which may exhibit different CO/Rh adsorption stoichiometries, the measured CO uptake was used as a comparative descriptor of the CO-accessible adsorption capacity rather than being directly converted into absolute Rh dispersion, active-metal surface area, or average Rh particle size.

4.3 Computational Details

Spin-polarized density functional theory (DFT) calculations were performed using the Vienna Ab initio Simulation Package (VASP). The projector-augmented-wave (PAW) method was employed to

Just Accepted

describe the interactions between the ionic cores and valence electrons, and the exchange-correlation interactions were treated using the PBE functional within the generalized gradient approximation (GGA). A plane-wave kinetic-energy cutoff of 400 eV was used. The electronic self-consistent calculations were converged to 1×10^{-4} eV, and structural optimizations were continued until the residual forces on all relaxed atoms were below 0.03 eV $Å^{-1}$. Brillouin-zone sampling was performed using a $1 \times 1 \times 1$ k-point mesh. A single-layer N-doped carbon model was constructed to represent the catalyst support. An isolated Rh atom coordinated with four N atoms was employed to represent the Rh single-atom site (Rhs). For the coupled single-atom–nanocluster model (Rhs–Rhc), a Rh_5 cluster, denoted as Rhc, was introduced adjacent to the $Rh–N_4$ site (Rhs). A three-layer Rh nanocrystal supported on the N-doped carbon model was constructed to represent the nanoparticle-dominated Rh environment (Rhn). A vacuum region of 15 Å was introduced perpendicular to the surface to minimize interactions between periodic images. These models were used as representative local Rh environments to investigate the effects of Rh nuclearity and coordination structure on molecular adsorption and elementary reaction steps, rather than as exact atomic representations of the experimentally synthesized catalysts. Given the structural complexity of the experimental catalysts, the present models do not explicitly account for the full distribution of pyridinic, pyrrolic, and graphitic N species, solvent effects, or the structural flexibility of the carbon support. Accordingly, the calculated adsorption energies and free-energy barriers are used primarily to compare relative trends among the representative Rh environments rather than as quantitatively exact energetics of the real catalysts.

The adsorption energy E_{ads} of H_2, CO, DIB, and other reaction species was calculated according to:

$$E_{ads} = E_{adsorbate+surface} - E_{surface} - E_{adsorbate} \quad , \qquad (1)$$

where $E_{adsorbate+surface}$, $E_{surface}$, and $E_{adsorbate}$ are the DFT total energies of the adsorbate–surface system, the clean catalyst surface, and the isolated adsorbate, respectively. According to this definition, a more negative E_{ads}indicates stronger exothermic adsorption.

Just Accepted

For the hydroformylation of DIB, the reaction pathway was constructed by considering the major elementary steps involved in aldehyde formation, including H_2 dissociation to generate surface Rh-H species, hydrogen insertion into adsorbed C_8H_{16} to form a Rh-C_8H_{17} alkyl intermediate, CO insertion into the Rh-C bond to generate the corresponding Rh-C_8H_{17}CO acyl intermediate, and the subsequent hydrogenation step leading to the C_9 aldehyde product. The corresponding elementary steps were examined on the Rhs, Rhs-Rhc, and Rhn models.

Transition states (TSs) for the elementary steps involved in DIB hydroformylation were searched using the climbing-image nudged elastic band (CI-NEB) method. Each transition state was further verified by vibrational-frequency analysis. A stable intermediate was confirmed by the absence of imaginary frequencies, whereas a transition state was identified by the presence of a single imaginary frequency corresponding to the expected reaction coordinate.

To obtain reaction energetics under conditions relevant to the catalytic experiments, thermodynamic corrections were evaluated at the experimental reaction temperature of 393.15 K. The Gibbs free energy of each intermediate and transition state was calculated according to: [31, 32, 33],

$$G(T) = E_{DFT} + E_{ZPE} + \Delta H_{Thermal}(T) - TS(T) \qquad (2)$$

where E_{DFT} is the electronic energy obtained from DFT calculations, E_{ZPE} is the zero-point-energy correction, $\Delta H_{\mathrm{thermal}}$ is the thermal enthalpy correction, and S is the entropy. Zero-point energies and vibrational thermodynamic corrections for surface-bound intermediates and transition states were obtained from the calculated vibrational frequencies within the harmonic approximation.

For gas-phase H_2 and CO, translational, rotational, and vibrational contributions were included in the thermodynamic corrections. Since the hydroformylation experiments were conducted under 6 MPa syngas with a CO/H_2 molar ratio of 1:1, the partial pressures of CO and H_2 were taken as 3 MPa each. The pressure-dependent chemical potential was corrected according to:

Just Accepted

$$\mu(T,p) = \mu(T,p^0) + RTln(\frac{p}{p^0}) \qquad (3)$$

where $p^\circ$is the standard pressure.

For each elementary step, the activation free-energy barrier was calculated from the difference between the Gibbs free energies of the corresponding transition state and initial state:

$$\Delta G = G_{TS} - G_{IS} \qquad (4)$$

where $G_{\mathrm{TS}}$and $G_{\mathrm{IS}}$are the Gibbs free energies of the transition state and its corresponding initial state, respectively. Taking the hydrogen insertion step involving adsorbed DIB on the Rhs model as an example, the activation free-energy barrier was calculated as:

$$\Delta G_{H-ins} = G_{TS-H} - G_{H+CO+C8H16-Rhs} \qquad (5)$$

where $G_{\mathrm{TS-H}}$is the Gibbs free energy of the transition state associated with hydrogen insertion into adsorbed C_8H_{16}, and $G_{\mathrm{H+CO+\ C_8H_{16}\ -Rhs}}$is the Gibbs free energy of the corresponding adsorbed initial state.

The reaction free energy for formation of the Rh–C_8H_{17} intermediate was calculated according to [34,35]:

$$\Delta G_{rxn} = G_{CO+C8H17-Rhs} - G_{H+CO+C8H16-Rhs} \qquad (6)$$

where $G_{\mathrm{CO+\ C_8H_{17}\ -Rhs}}$ represents the Gibbs free energy of the Rh–C_8H_{17} intermediate. The same procedure was applied to CO insertion, subsequent hydrogenation, and the corresponding elementary steps on the Rhs–Rhc and Rhn models. Unless otherwise specified, all Gibbs free energies and activation free-energy barriers discussed herein refer to values evaluated at 393.15 K.

Data availability

All data needed to support the conclusions in the paper are presented in the manuscript and the Electronic Supplementary Material. Additional data related to this paper may be requested from the corresponding author upon request.

Acknowledgements

This work was supported by the National Natural Science Foundation of China (No. 22572206), the Shandong Province Key Research and Development Plan, China (2023CXGC010607), and the Natural Science Foundation of Shandong Province (ZR2023ZD23).

Just Accepted

Declaration of competing interest

All the contributing authors report no conflict of interests in this work.

Author contribution statement

Pengzhen Yin: Conceptualization, Methodology, Data Curation, Formal analysis, Investigation, Visualization, Writing-Original Draft, Writing-Review & Editing. Chao Feng: Methodology, Data Curation, DFT calculation. Shingo Hasegawa: Data Curation, Formal analysis. Ken Motokura: Data Curation, Formal analysis, Supervision. Yifan Liu, Yi Zhang, Yudi Wu, Zhaozhan Wang: Data Curation, Formal analysis. Yong Yang: Conceptualization, Funding acquisition, Project administration, Supervision, Writing-Original Draft, Writing-Review & Editing. All the authors have approved the final manuscript.

Informed consent

Not applicable

Ethics statement

Not applicable

Use of AI statement

None

References

[1] Liu, B. Y.; Wang, Y.; Huang, N.; Lan, X. C.; Xie, Z. H.; Chen, J. G. G.; Wang, T. F. Heterogeneous hydroformylation of alkenes by Rh-based catalysts. *Chem* **2022**, *8*, 2630−2658.

[2] Zhang, X. J.; Yan, T.; Hou, H. M.; Yin, J. Q.; Wan, H. L.; Sun, X. D.; Zhang, Q.; Sun, F. F.; Wei, Y.; Dong, M.; Fan, W. B.; Wang, J. G.; Sun, Y. J.; Zhou, X.; Wu, K.; Yang, Y.; Li, Y. W.; Cao, Z. Regioselective hydroformylation of propene catalysed by rhodium-zeolite. *Nature* **2024**, *629*, 597−602.

[3] Franke, R.; Selent, D.; Börner, A. Applied hydroformylation. *Chem. Rev.* **2012**, *112*, 5675−5732.

[4] Qi, L.; Das, S.; Zhang, Y. S.; Nozik, D.; Gates, B. C.; Bell, A. T. Ethene hydroformylation catalyzed by rhodium dispersed with zinc or cobalt in silanol nests of dealuminated zeolite beta. *J. Am. Chem. Soc*. **2023**, *145*, 2911−2929.

[5] Samanta, P.; Solé-Daura, A.; Rajapaksha, R.; Wisser, F. M.; Meunier, F.; Schuurman, Y.; Sassoye, C.; Mellot-Draznieks, C.; Canivet, J. Heterogenized molecular rhodium phosphine catalysts within metal-organic frameworks for alkene hydroformylation. *ACS Catal*. **2023**, *13*, 4193−4204.

[6] Bauer, G.; Ongari, D.; Tiana, D.; Gäumann, P.; Rohrbach, T.; Pareras, G.; Tarik, M.; Smit, B.; Ranocchiari, M. Metal-organic frameworks as kinetic modulators for branched selectivity in hydroformylation. *Nat. Commun*. **2020**, *11*, 1059.

[7] Birkelbach, K. V. A.; Vossen, J. T.; Rösler, T.; Kappel, I.; Meise, A.; Heggen, M.; Vorholt, A. J.; Palkovits, R. An immobilized Rh-based solid molecular catalyst for the reductive hydroformylation of 1-octene. *Angew. Chem. Int. Ed*. **2025**, *64*, e202424144.

[8] Wang, Y. Q.; Yan, L.; Li, C. Y.; Jiang, M.; Wang, W. L.; Ding, Y. J. Highly efficient porous organic copolymer supported Rh catalysts for heterogeneous hydroformylation of butenes. *Appl. Catal. A: Gen*. **2018**, *551*, 98−105.

[9] Feng, S. Q.; Jiang, M.; Song, X. G.; Qiao, P. Z.; Yan, L.; Cai, Y. T.; Li, B.; Li, C. Y.; Ning, L. L.; Liu, S. Y.; Zhang, W. Q.; Wu, G. R.; Yang, J. Y.; Dong, W. R.; Yang, X. M.; Jiang, Z.; Ding, Y. J. Sulfur poisoning and self-recovery of single-site Rh1/porous organic polymer catalysts for olefin hydroformylation. *Angew. Chem. Int. Ed*. **2023**, *62*, e202304282.

[10] Riisager, A.; Fehrmann, R.; Flicker, S.; van Hal, R.; Haumann, M.; Wasserscheid, P. Very stable and highly regioselective supported ionic-liquid-phase (SILP) catalysis: continuous-flow fixed-bed hydroformylation of propene.

Just Accepted

Angew. Chem. Int. Ed. **2005**, *44*, 815−819.
[11] Liu, B. Y.; Wang, Y.; Huang, N.; Lan, X. C.; Wang, T. F. Activity promotion of $Rh_{8-x}Co_xP_4$ bimetallic phosphides in styrene hydroformylation: dual influence of adsorption and surface reaction. *ACS Catal*. **2021**, *11*, 9850−9859.
[12] Kamran, M.; Qadir, S.; Bai, C. Z.; Sajjad, M.; Ramki, K.; Dharani, S.; Zheng, Z. Y.; Su, X.; Bai, S. T. Encapsulated heterogeneous rhodium single-atom catalysts for linear selective hydroformylation of 1-octene. *Small* **2025**, *21*, e08765.
[13] Jeevanandham, S.; Maji, A.; Kumari, N.; Gu, B. S.; No, J.; Choi, H. C.; Oh, D.; An, K.; Kumar, A.; Lee, I. S. Ligand-substrate self-sorting in silica-encased Rh-nanopetals as model catalyst for hydroformylation of arylalkenes. *Nano Lett*. **2025**, *25*, 15970−15977.
[14] Mao, Z. T.; Xie, Z. H.; Chen, J. G. Comparison of heterogeneous hydroformylation of ethylene and propylene over $RhCo_3$/MCM-41 catalysts. *ACS Catal*. **2021**, *11*, 14575−14585.
[15] Wang, L. B.; Zhang, W. B.; Wang, S. P.; Gao, Z. H.; Luo, Z. H.; Wang, X.; Zeng, R.; Li, A. W.; Li, H. L.; Wang, M. L.; Zheng, X. S.; Zhu, J. F.; Zhang, W. H.; Ma, C.; Si, R.; Zeng, J. Atomic-level insights in optimizing reaction paths for hydroformylation reaction over Rh/CoO single-atom catalyst. *Nat. Commun*. **2016**, *7*, 14036.
[16] Amsler, J.; Sarma, B. B.; Agostini, G.; Prieto, G.; Plessow, P. N.; Studt, F. Prospects of heterogeneous hydroformylation with supported single atom catalysts. *J. Am. Chem. Soc*. **2020**, *142*, 5087−5096.
[17] Lang, R.; Li, T. B.; Matsumura, D.; Miao, S.; Ren, Y. J.; Cui, Y. T.; Tan, Y.; Qiao, B. T.; Li, L.; Wang, A. Q.; Wang, X. D.; Zhang, T. Hydroformylation of olefins by a rhodium single-atom catalyst with activity comparable to $RhCl(PPh_3)_3$. *Angew. Chem. Int. Ed*. **2016**, *55*, 16054−16058.
[18] Dou, X. M.; Yan, T.; Li, W. Y.; Zhu, C. F.; Chen, T. X.; Lo, B. T. W.; Marini, C.; Xiao, H.; Liu, L. C. Structure-reactivity relationship of zeolite-confined Rh catalysts for hydroformylation of linear α-olefins. *J. Am. Chem. Soc*. **2025**, *147*, 2726−2736.
[19] Zhao, M. J.; Li, C. G.; Gómez, D.; Gonell, F.; Diaconescu, V. M.; Simonelli, L.; Haro, M. L.; Calvino, J. J.; Meira, D. M.; Concepción, P.; Corma, A. Low-temperature hydroformylation of ethylene by phosphorous stabilized Rh sites in a one-pot synthesized Rh-(O)-P-MFI zeolite. *Nat. Commun*. **2023**, *14*, 7174.
[20] Dou, X. M.; Yan, T.; Qian, L. X.; Hou, H. M.; Haro, M. L.; Marini, C.; Agostini, G.; Meira, D. M.; Zhang, X. J.; Zhang, L.; Cao, Z.; Liu, L. C. Regioselective hydroformylation with subnanometre Rh clusters in MFI zeolite. *Nat. Catal*. **2024**, *7*, 666−677.
[21] Hu, H. C.; Cui, W. H.; Gao, M. B.; Wang, L. Y.; Liu, S. P.; Qi, L.; Yan, W. F.; Tian, P.; Liu, Z. M. Construction of zeolite framework-anchored Rh-$(O\text{-}Zn)_x$ sites for hydroformylation of olefins. *J. Am. Chem. Soc*. **2025**, *147*, 34381−34394.
[22] Gao, P.; Liang, G. F.; Ru, T.; Liu, X. Y.; Qi, H. F.; Wang, A. Q.; Chen, F. E. Phosphorus coordinated Rh single-atom sites on nanodiamond as highly regioselective catalyst for hydroformylation of olefins. *Nat. Commun*. **2021**, *12*, 4698.
[23] Liu, L. C.; Corma, A. Confining isolated atoms and clusters in crystalline porous materials for catalysis. *Nat. Rev. Mater*. **2021**, *6*, 244−263.
[24] Zhang, K.; Dou, X. M.; Hou, H. M.; Zhou, Z. Y.; Lopez-Haro, M.; Meira, D. M.; Liu, P.; He, P.; Liu, L. C. Generation of subnanometer metal clusters in silicoaluminate zeolites as bifunctional catalysts. *JACS Au* **2023**, *3*, 3213−3226.
[25] Yu, Z. N.; Zhang, S. X.; Zhang, L. L.; Liu, X. Y.; Jia, Z. H.; Li, L.; Ta, N.; Wang, A.; Liu, W.; Wang, A. Q.; Zhang, T. Suppressing metal leaching and sintering in hydroformylation reaction by modulating the coordination of Rh single atoms with reactants. *J. Am. Chem. Soc*. **2024**, *146*, 11955−11967.
[26] Sarma, B. B.; Neukum, D.; Doronkin, D. E.; Nilayam, A. R. L.; Baumgarten, L.; Krause, B.; Grunwaldt, J. D. Understanding the role of supported Rh atoms and clusters during hydroformylation and CO hydrogenation reactions with in situ/operando XAS and DRIFT spectroscopy. *Chem. Sci.* **2024**, *15*, 12369−12379.
[27] Schuster, M. L.; Peterson, K. P.; Stoffregen, S. A. Isobutylene dimerization: a discovery-based exploration of mechanism and regioselectivity by NMR spectroscopy and molecular modeling. *J. Chem. Educ.* **2018**, *95*, 1040−1044.
[28] Karinen, R. S.; Lylykangas, M. S.; Krause, A. O. I. Reaction equilibrium in the isomerization of 2,4,4-trimethyl pentenes. *Ind. Eng. Chem. Res*. **2001**, *40*, 1011−1015.

Just Accepted

[29] Busca, G. Acid catalysts in industrial hydrocarbon chemistry. *Chem. Rev.* **2007**, *107*, 5366−5410.
[30] Bohnen, H. W.; Cornils, B. Hydroformylation of alkenes: an industrial view of the status and importance. *Adv. Catal*. **2002**, *47*, 1−64.
[31] Kresse, G.; Furthmüller, J. Efficient iterative schemes for ab initio total-energy calculations using a plane-wave basis set. *Phys. Rev. B* **1996**, *54*, 11169−11186.
[32] Perdew, J. P.; Burke, K.; Ernzerhof, M. Generalized gradient approximation made simple. *Phys. Rev. Lett.* **1996**, *77*, 3865−3868.
[33] Kresse, G.; Joubert, D. From ultrasoft pseudopotentials to the projector augmented-wave method. *Phys. Rev. B* **1999**, *59*, 1758−1775.
[34] Henkelman, G.; Uberuaga, B. P.; Jónsson, H. A climbing image nudged elastic band method for finding saddle points and minimum energy paths. *J. Chem. Phys*. **2000**, *113*, 9901−9904.
[35] Campbell, C. T.; Sellers, J. R. V. The entropies of adsorbed molecules. *J. Am. Chem. Soc*. **2012**, *134*, 18109−18115.
[36] Wang, Y.; Chen, M. T.; Zhang, K. Y.; Wu, H. M.; Wang, J. L.; Cheng, Y. R.; Liu, Y. X.; Wei, Z. J. CoNi alloy nanoparticles confined in N-doped porous carbon as an efficient and versatile catalyst for reductive amination of levulinic acid/esters to N-substituted pyrrolidones. *ACS Catal*. **2023**, *13*, 12601−12616.
[37] Chen, Y. J.; Zhang, R. X.; Chen, Z. W.; Liao, J. W.; Song, X. D.; Liang, X.; Wang, Y.; Dong, J. C.; Singh, C. V.; Wang, D. S.; Li, Y. D.; Toste, F. D.; Zhao, J. Heterogeneous rhodium single-atom-site catalyst enables chemoselective carbene N-H bond insertion. *J. Am. Chem. Soc*. **2024**, *146*, 10847−10856.
[38] Liu, Y. F.; Liu, Z. Q.; Hui, Y.; Wang, L.; Zhang, J.; Wang, C. T.; Wang, H.; Qin, Y. C.; Song, L. J.; Zheng, A. M.; Xiao, F. S. Rhodium nanoparticles supported on silanol-rich zeolites beyond the homogeneous Wilkinson's catalyst for hydroformylation of olefins. *Nat. Commun*. **2023**, *14*, 2531.
[39] Li, B.; Mu, J. L.; Long, G. F.; Song, X. G.; Zhao, Y.; Huang, E. D.; Liu, S. Y.; Wei, Y.; Sun, F. F.; Feng, S. Q.; Yuan, Q.; Li, X. J.; Cai, Y. T.; Zhang, Y.; Dong, W. R.; Zhang, W. Q.; Yang, X. M.; Deng, D. H.; Yan, L.; Ding, Y. J. Directly oxidizing ethanol to glycolic acid over a single-Rh-site catalyst via water-mediated oxygen shuttle. *J. Am. Chem. Soc.* **2025**, *147*, 29052−29064.
[40] Wang, S. C.; Guo, Z. C.; Wang, L. R.; Zeng, Y. J.; Liang, X.; Dong, F.; Zhu, P. D.; Liu, H. F.; Wang, D. S.; Li, Y. D. Atomically dispersed palladium catalyst for chemoselective hydrogenation of quinolines. *Nano Lett*. **2024**, *24*, 12666−12675.
[41] Yang, D.; Tao, S.; Zhu, H. Y.; Wang, Z. D.; Gao, W. W.; Yu, J. G.; Wang, M. M.; Sun, G. X.; Li, J. X.; Chen, H. C.; Liu, B.; Chai, Y. M.; Pan, Y. Construction of Rh-N_4 single atoms and Rh clusters dual-active sites for synergistic heterogeneous hydroformylation of olefins with ultra-high turnover frequency. *Chem. Eng. J*. **2024**, *479*, 147505.
[42] Hadjiivanov, K. I.; Vayssilov, G. N. Characterization of oxide surfaces and zeolites by carbon monoxide as an IR probe molecule. *Adv. Catal*. **2002**, *47*, 307−511.
[43] Zhou, X.; Zhao, Y. J.; Yin, P. Z.; Wang, Z. Z.; Zhao, X. T.; Zhang, F. Q.; Shi, H. B.; Gorbunov, D.; Yang, Y. Regioselective hydroformylation of sterically hindered olefins over single-atom Rh sites on porous organic polymer incorporating hybrid phosphine ligands. *J. Catal*. **2025**, *452*, 116439.
[44] Matsubu, J. C.; Yang, V. N.; Christopher, P. Isolated metal active site concentration and stability control catalytic CO_2 reduction selectivity. *J. Am. Chem. Soc*. **2015**, *137*, 3076−3084.
[45] Oh, D. W.; Kim, M. Y.; Lee, H. J.; Bae, J. S.; Jeong, B. G.; Hur, C. H.; Han, J. W.; An, K. J. Rh cluster catalysts with enhanced catalytic activity: the Goldilocks Rh size for olefin hydroformylation. *ACS Catal*. **2025**, *15*, 21088−21099.
[46] Wang, Y. Y.; Zhang, M. Y.; Zhao, L.; Liu, D. R.; Liu, C.; Wang, J. W.; Wang, Q.; Xu, G. Y.; He, H. Rh atomic clusters on CeO_2 promote water activation for ethanol steam reforming. *Appl. Catal. B Environ. Energy* **2026**, *399*, 127116.
[47] Suen, D. W.-S.; Li, C.-Y. V.; Sun, X.; Chen, J.; Yang, C.; Qiu, M.; Lu, X.-Y.; Wang, B.; Niu, S.; Liu, W.; Tsang, C.-W. Dual-active site engineering of Co/Cu single atoms and nanoclusters on M-Nx-CNTs (M = Co, Cu, CoCu): Synergistic catalysis for ultrafast hydrogen production from ammonia borane. *J. Colloid Interface Sci.* **2025**, *700*, 138560.
Just Accepted

[48] Yin, P. Q.; Yao, T.; Wu, Y.; Zheng, L. R.; Lin, Y.; Liu, W.; Ju, H. X.; Zhu, J. F.; Hong, X.; Deng, Z. X.; Zhou, G.; Wei, S. Q.; Li, Y. D. Single cobalt atoms with precise N-coordination as superior oxygen reduction reaction catalysts. *Angew. Chem. Int. Ed*. **2016**, *55*, 10800−10805.

[49] Qu, Y. T.; Li, Z. G.; Chen, W. X.; Lin, Y.; Yuan, T.; Yang, Z. B.; Zhao, C.; Wang, J.; Zhao, C. G.; Wang, X.; Zhou, J.; Zhuang, Z. B.; Wu, Y.; Li, Y. D. Direct transformation of bulk copper into copper single sites via emitting and trapping of atoms. *Nat. Catal*. **2018**, *1*, 781−786.

[50] Liu, S. X.; Lin, S. Y.; Nie, K. Q.; Huai, M. J.; Kang, Z. Y.; Lan, X. C.; Xiang, L.; Wang, T. F. Tuning extrinsic stability of rhodium catalysts in heterogeneous hydroformylation. *ACS Catal*. **2026**, *16*, 7002−7012.

[51] Taherkhani, F.; Mauss, F. CO adsorption on Pt, Rh, and Pt−Rh fuel cell nanocatalysts supported on bilayer graphene from the metal-to-amorphous phase transition. *Precis. Chem*. **2026**, doi: 10.1021/prechem.6c00087.

[52] Xia, D.; Wang, H.; Li, B.; Lu, B.; Wang, Y.; Mao, S. J. Enhancing hydroformylation activity and stability of Rh-based catalysts through Ni and P incorporation. *J. Catal*. **2026**, *456*, 116782.

[53] Ro, I. S.; Xu, M. J.; Graham, G. W.; Pan, X. Q.; Christopher, P. Synthesis of heteroatom Rh-ReO_x atomically dispersed species on Al_2O_3 and their tunable catalytic reactivity in ethylene hydroformylation. *ACS Catal*. **2019**, *9*, 10899−10912.

Just Accepted

Electronic Supplementary Material

Neighboring Rh nanoclusters promote the activity and stability of Rh single-atom catalyst for the hydroformylation of sterically hindered diisobutylene

Pengzhen Yin[1,4,§], Chao Feng[2,§], Shingo Hasegawa[3], Ken Motokura[3], Yifan Liu[1,4], Yi Zhang[1], Yudi Wu[1], Zhaozhan Wang[1,5], Yong Yang[1,4,5]*

[1] *Key Laboratory of Photoelectric Conversion and Utilization of Solar Energy, Qingdao Institute of Bioenergy and Bioprocess Technology, Chinese Academy of Sciences, Qingdao 266101, China*

[2] *College of Chemical and Biological Engineering, Shandong University of Science and Technology, Qingdao 266590, China*

[3] *Department of Chemistry and Life Science, Yokohama National University, Yokohama 20-8501, Japan*

[4] *University of Chinese Academy of Sciences, Beijing 100049, China*

[5] *Present address: College of Chemical Engineering, Qingdao University of Science and Technology, Qingdao 266042, China*

[§] Pengzhen Yin and Chao Feng contributed equally to this work.

Address correspondence to yangyong@qibebt.ac.cn, yangyong@qust.edu.cn

Supporting information to https://doi.org/10.26599/NR.2026.94909264

Just Accepted

This PDF file contains

Figure S1 – S16

Table S1 – S5

Additional Results and Discussion

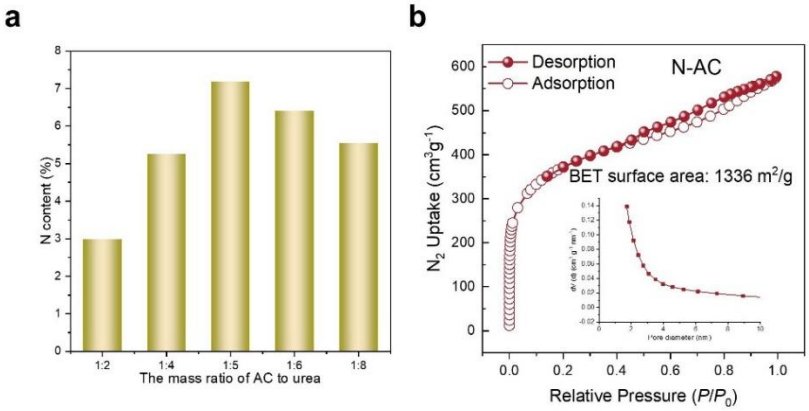


Figure S1. (a) Optimization of the nitrogen content (wt%) in the N-AC support as a function of the initial AC/urea mass ratio. (b) N_2 adsorption–desorption isotherms at 77 K for the optimized N-AC (1:5) support. The inset shows the corresponding pore-size distribution derived from the desorption branch.

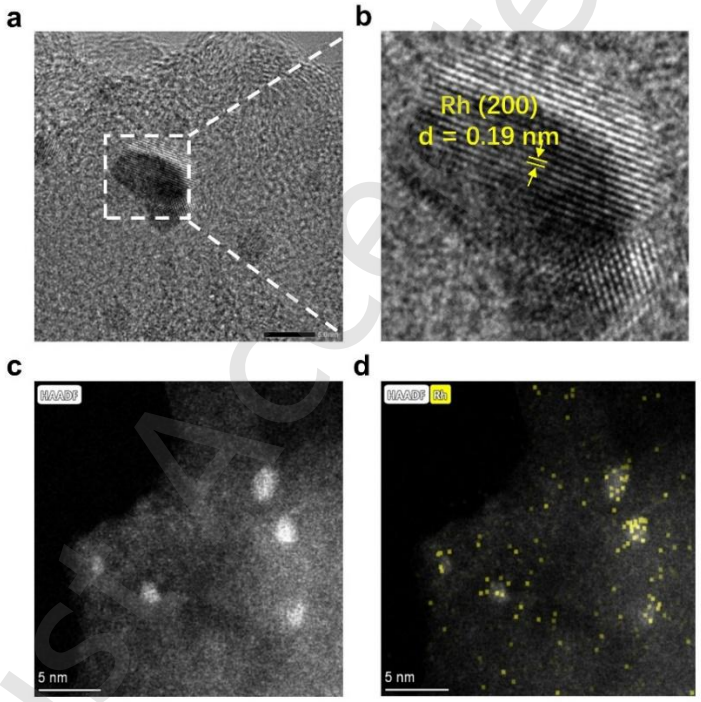


Figure S2. (a) HRTEM image of a Rh nanoparticle in Rh/N-AC-650. (b) Magnified HRTEM image of the nanoparticle in (a), showing well-resolved lattice fringes with a d-spacing of 0.19 nm corresponding to the Rh(200) plane of face-centered cubic (fcc) Rh. (c) Aberration-corrected HAADF-STEM image of Rh/N-AC-650. (d) Corresponding EDS elemental mapping of Rh.

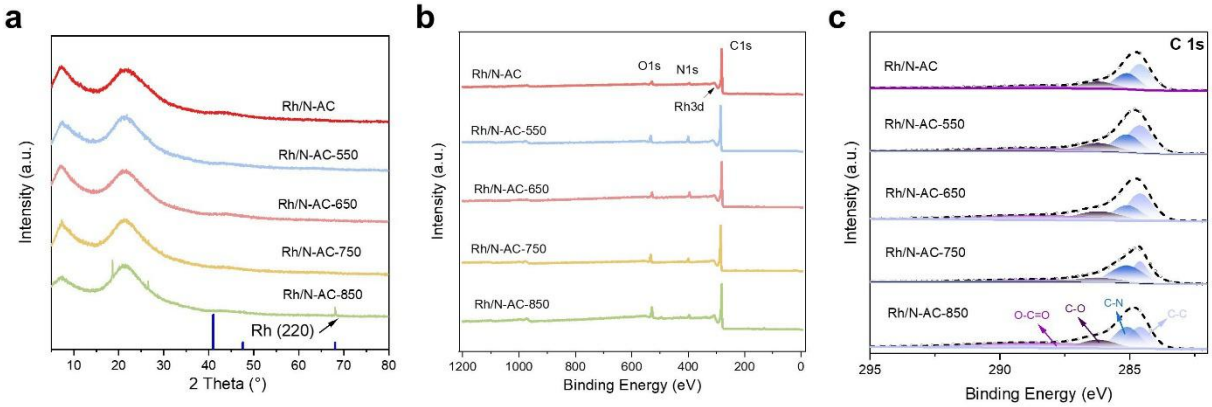


Figure S3. (a) XRD patterns of the Rh/N-AC-T catalysts prepared at different calcination temperatures. (b) XPS survey

spectra and (c) high-resolution C 1s XPS spectra of the Rh/N-AC-T catalysts.

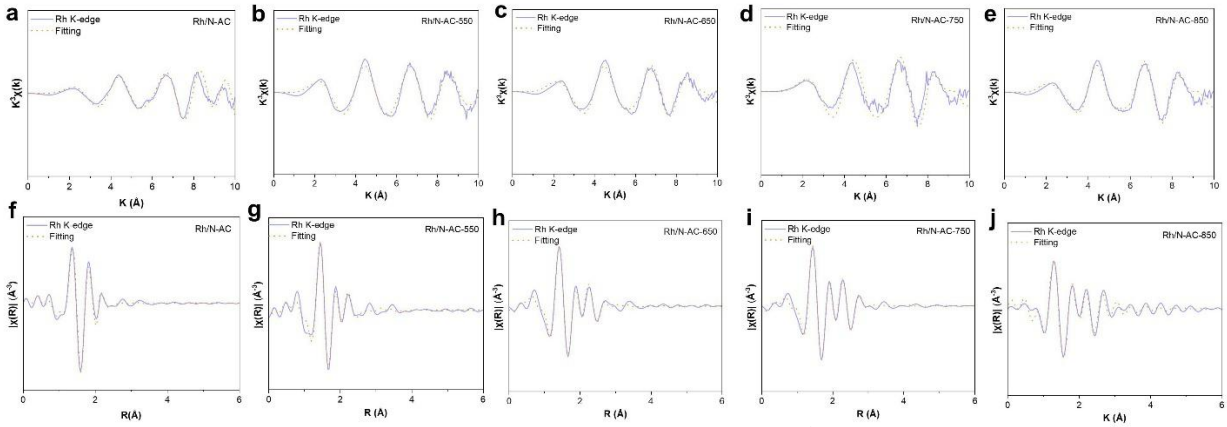


Figure S4. k-space fitting curves (a–e) and R-space fitting curves (f–j): (a, f) Rh/N-AC, (b, g) Rh/N-AC-550, (c, h) Rh/N-AC-650, (d, i) Rh/N-AC-750, and (e, j) Rh/N-AC-850.

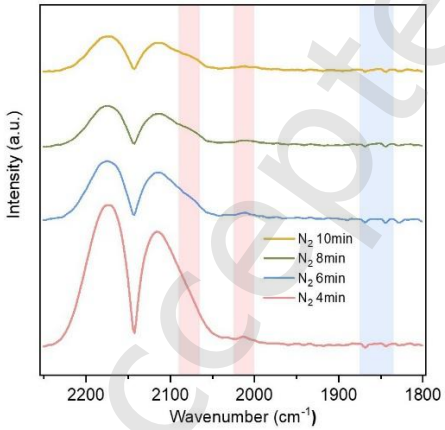


Figure S5. Time-resolved in situ CO-DRIFTS spectra of Rh/N-AC-650 recorded during N_2 purging at room temperature after CO adsorption. The catalyst was pretreated in N_2 at 120 °C for 60 min, followed by CO adsorption using a CO/N_2 mixture (1:19, v/v; total flow rate, 15 mL·min^{-1}) at room temperature for 60 min. After adsorption, the gas feed was switched to pure N_2 (15 mL·min^{-1}) for purging at room temperature.

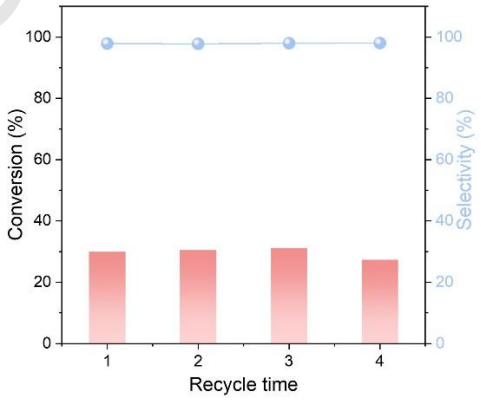


Figure S6. Recycling stability of Rh/N-AC-650 under low-conversion hydroformylation conditions.

Just Accepted

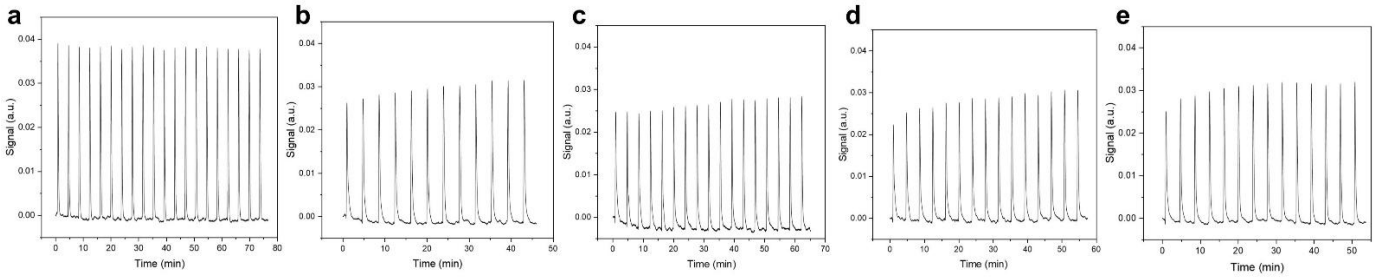


Figure S7. CO pulse chemisorption response curves of (a) Rh/N-AC, (b) Rh/N-AC-550, (c) Rh/N-AC-650, (d) Rh/N-AC-750, and (e) Rh/N-AC-850.

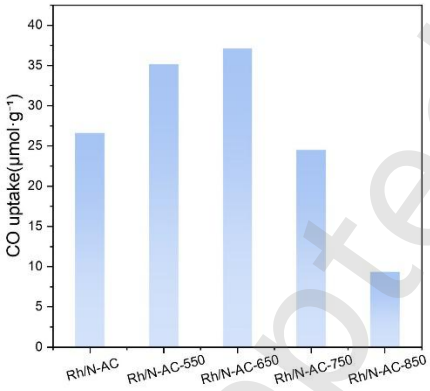


Figure S8. CO uptake of Rh/N-AC catalysts determined by CO pulse chemisorption.

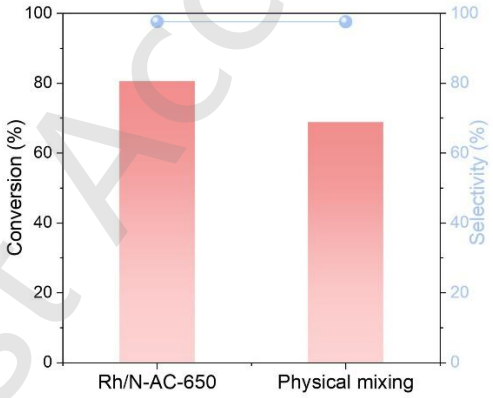


Figure S9. Comparison of DIB conversion and aldehyde selectivity over Rh/N-AC-650 and the physical-mixture control composed of Rh/N-AC and Rh/N-AC-700. Reaction conditions: DIB, 6.38 mmol; catalyst, 40 mg; toluene, 10 mL; 120 °C; 6 MPa syngas (CO/H_2 = 1:1, v/v); 6 h.

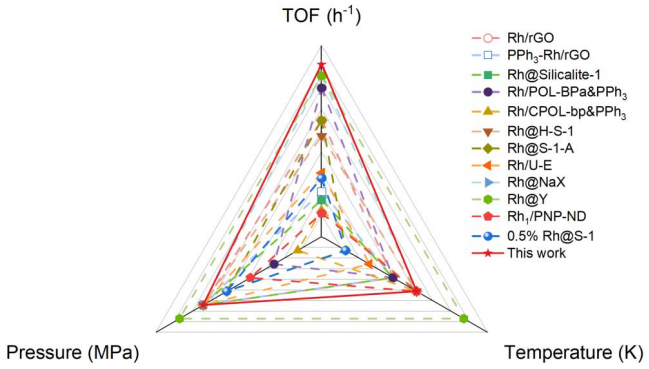


Figure S10. Comparison of Rh/N-AC-650 with previously reported heterogeneous Rh catalysts for olefin hydroformylation [1–12]. The reported TOF values were obtained under different reaction conditions, including reaction temperature, syngas pressure, substrate, catalyst formulation, and other experimental parameters; therefore, this comparison is intended as a contextual benchmark rather than a strict like-for-like evaluation of catalytic activity.

Just Accepted

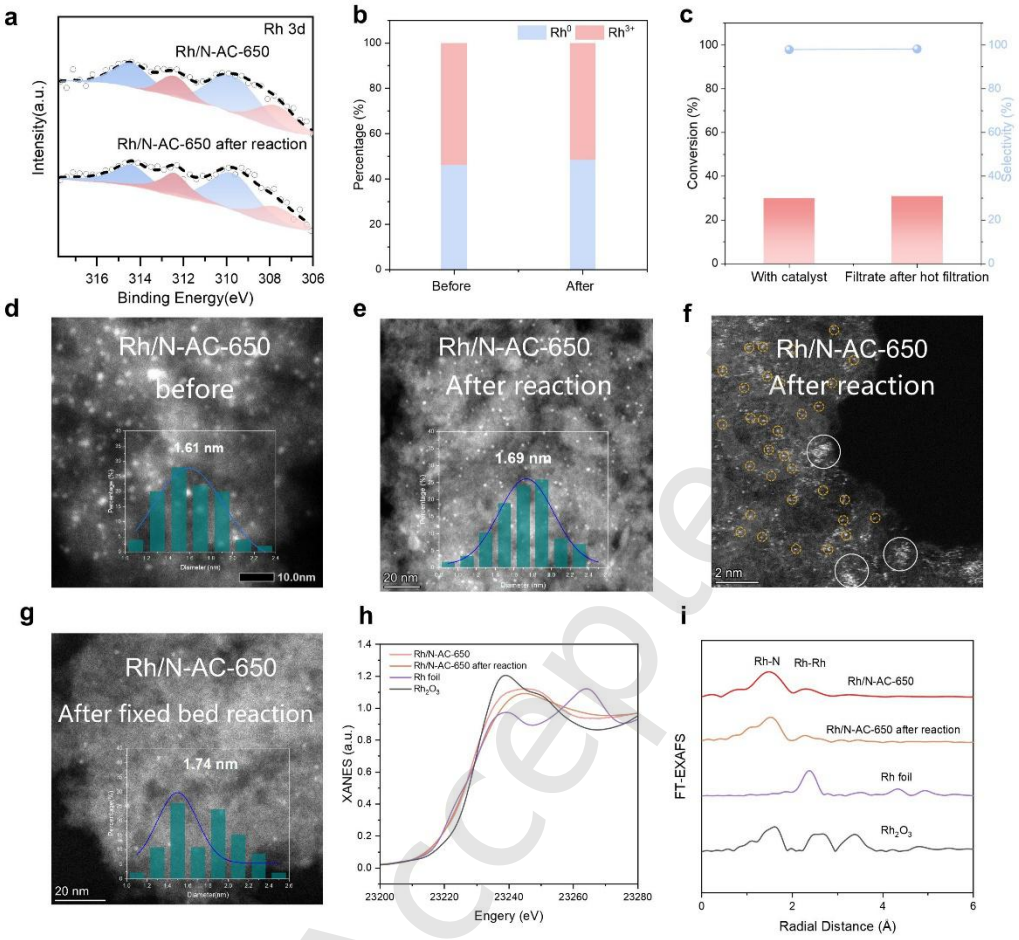


Figure S11. (a) High-resolution Rh 3d XPS spectra of fresh Rh/N-AC-650 and Rh/N-AC-650 after four recycling runs. (b) Relative proportions of Rh^0 and Rh^{3+} species derived from Rh 3d XPS deconvolution for fresh Rh/N-AC-650 and Rh/N-AC-650 after four recycling runs. (c) Hot-filtration experiment over Rh/N-AC-650, showing no appreciable further conversion after removal of the solid catalyst. (d) HAADF-STEM image and corresponding Rh particle-size distribution of fresh Rh/N-AC-650. (e) HAADF-STEM image and corresponding Rh particle-size distribution of Rh/N-AC-650 after four recycling runs. (f) AC-HAADF-STEM image of Rh/N-AC-650 after reaction; atomically dispersed Rh single atoms and Rh nanoclusters are marked by yellow and white circles, respectively. (g) HAADF-STEM image and corresponding Rh particle-size distribution of Rh/N-AC-650 after the long-term fixed-bed reaction. (h) Rh K-edge XANES spectra of Rh/N-AC-650 before and after reaction, together with Rh foil and Rh_2O_3 references. (i) FT-EXAFS R-space profiles of Rh/N-AC-650 before and after reaction, together with Rh foil and Rh_2O_3 references.

Just Accepted

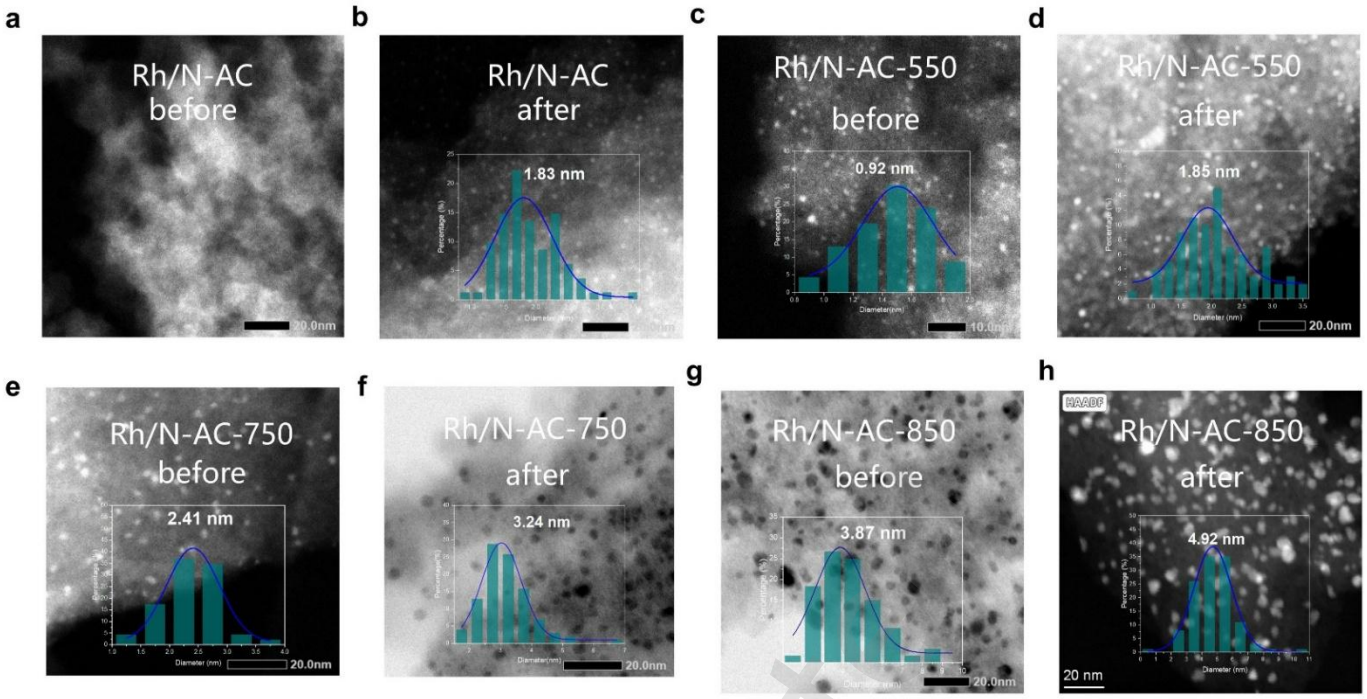


Figure S12. HAADF-STEM images and corresponding Rh particle size distributions for the (a) Rh/N-AC, (b) Rh/N-AC after four recycling runs, (c) Rh/N-AC-550, (d) Rh/N-AC-550 after four recycling runs, (e) Rh/N-AC-750, (f) Rh/N-AC-750 after four recycling runs, (g) Rh/N-AC-850, and (h) Rh/N-AC-850 after four recycling runs.

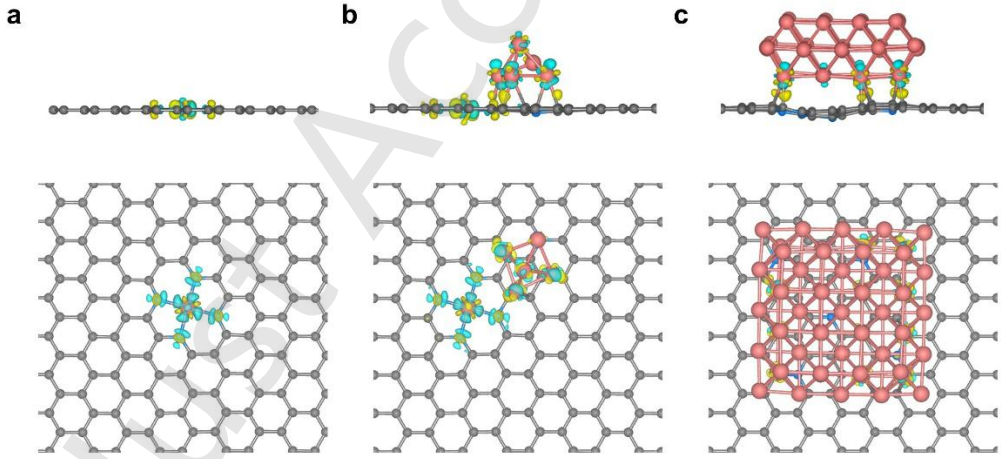


Figure S13. Charge density difference plot for (a) Rhs, (b) Rhs–Rhc, and (c) Rhn. The isosurface value is 0.01 e·Bohr-3. Yellow is positive and blue is negative.

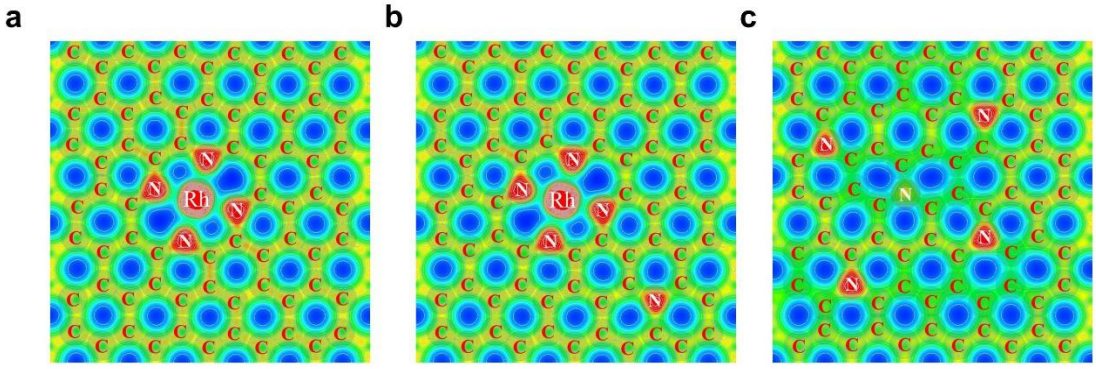


Figure S14. Electron localization function (ELF) maps for (a) Rhs, (b) Rhs–Rhc, and (c) Rhn.

Just Accepted

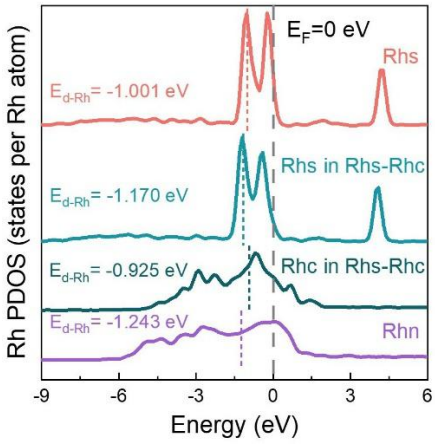


Figure S15. Projected density of states (PDOS) of the Rh 3d states for Rhs, Rhs in Rhs–Rhc, Rhc in Rhs–Rhc, and Rhn. Dashed lines indicate the corresponding calculated d-band centers, with the values indicated in each panel.

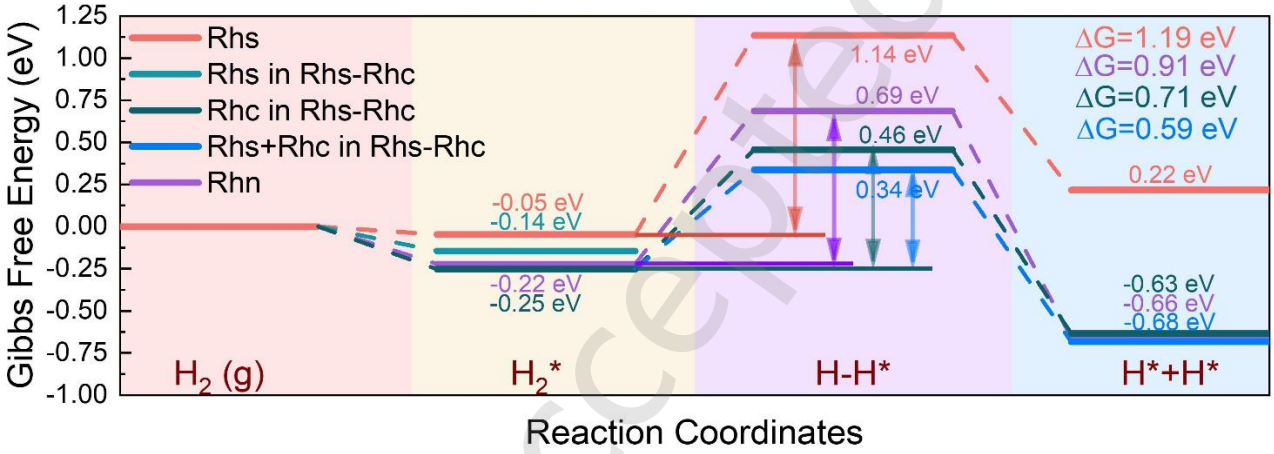


Figure S16. Gibbs free-energy profiles for H_2 dissociation at different sites in the Rhs, Rhs–Rhc, and Rhn models.

Table S1. Rhodium and nitrogen contents of different types of catalysts.

Entry	Catalyst	Rh content(wt%)	N content(wt%)
1	Rh/N-AC	0.43	7.10
2	Rh/N-AC-550	0.42	6.94
3	Rh/N-AC-650	0.41	6.63
4	Rh/N-AC-750	0.40	5.72
5	Rh/N-AC-850	0.40	4.23

Just Accepted

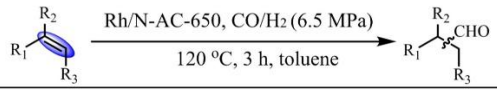
Table S2. EXAFS fitting results for the Rh/N-AC-T catalysts.

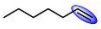
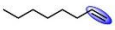
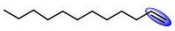
Sample	Path	CN	R (Å)	σ^2 ($Å^2$)	ΔE_0 (eV)	R-factor
Rh/N-AC	Rh-N	5.6	2.01	0.0065	1.2	0.0023
Rh/N-AC-550	Rh-N	4.0	2.03	0.0059	1.4	0.019
	Rh-Rh	1.75	2.67	0.0085	1.4	
Rh/N-AC-650	Rh-N	4.0	2.02	0.0072	1.8	0.017
	Rh-Rh	2.75	2.68	0.0066	1.8	
Rh/N-AC-750	Rh-N	4.0	2.01	0.0032	1.4	0.019
	Rh-Rh	4.25	2.70	0.0064	1.4	
Rh/N-AC-850	Rh-N	4.0	2.04	0.0069	1.3	0.017
	Rh-Rh	6	2.70	0.0095	1.3	
Rh foil	Rh-Rh	12	2.68	0.00298	1.7	0.007
Rh_2O_3	Rh-O	6	2.05	0.00147	1.5	0.020

R range: 1.0–3.0 Å; k range: 3.0–14.0 Å. CN, coordination number; R, bond distance; σ^2, Debye–Waller factor; ΔE_0 , inner potential correction; R-factor, goodness of fit. The estimated uncertainties of the fitted structural parameters are ±20% for CN, ±1% for R, and ±20% for σ^2.

Just Accepted

Table S3. Substrate scope of alkenes for hydroformylation.



Entry [a]	Substrate	Conv. (%)	Yield (%)	l/b	TOF (h^{-1})
1		96.5	95.5	1.07	3606
2[b]		83.4	77.1	Only 1	689
3		95.8	94.8	1.07	3125
4		93.4	92.5	1.04	2192
5		95.3	94.3	1.09	1538
6		95.3	94.3	1.27	2609
7[c]		63.1	63.1	1.2	1353
8		99	99	Only 1	4202
9[b]		78.6	73.9	Only 1	649
10[d]		69	68.1	0.82	7035
11		98.9	97.9	0.65	3014
12		97.8	96.8	0.59	2681
13		96.6	95.6	0.58	2192
14		95.3	94.3	0.54	1844

a Standard reaction conditions: olefin, 6.38 mmol; Rh/N-AC-650, 40 mg; toluene, 10 mL; 120 °C; 3 h; 6.5 MPa syngas (CO/H_2 = 1:1). b Reaction time: 6 h. c Reaction time: 1.5 h. d Reaction conditions: olefin, 8 mmol; Rh/N-AC-650, 20 mg; toluene, 10 mL; 100 °C; 1 h; 5 MPa syngas (CO/H_2 = 1:1). The l/b value represents the ratio of linear to branched aldehydes.

Table S4. Rh contents of the catalysts before and after four recycling runs.

Entry	**Catalyst**	**Rh content(wt%)**	**Rh content after 4 recycle(wt%)**
1	Rh/N-AC-650	0.41	0.38
2	Rh/N-AC-850	0.40	0.22

Just Accepted

Table S5. Average Bader charge and average state values of Rhs, Rhs in Rhs–Rhc, Rhc in Rhs–Rhc, and Rhn.

Sample	Structure	Average Bader charge	Average state value
Rhs	Rhs	14.323	1.355
Rhs-Rhc	Rhs	14.333	1.334
	Rhc	14.918	0.082
Rhn	Rhn	14.985	0.015

References:

[1] Gao, P.; Liang, G. F.; Ru, T.; Liu, X. Y.; Qi, H. F.; Wang, A. Q.; Chen, F. E. Phosphorus coordinated Rh single-atom sites on nanodiamond as highly regioselective catalyst for hydroformylation of olefins. *Nat. Commun.* **2021**, *12*, 4698.

[2] Tan, M. H.; Ishikuro, Y.; Hosoi, Y.; Yamane, N.; Ai, P. P.; Zhang, P. P.; Yang, G. H.; Wu, M. B.; Yang, R. Q.; Tsubaki, N. PPh_3 functionalized Rh/rGO catalyst for heterogeneous hydroformylation: bifunctional reduction of graphene oxide by organic ligand. *Chem. Eng. J*. **2017**, *330*, 863−869.

[3] Li, C. Y.; Sun, K. J.; Wang, W. L.; Yan, L.; Sun, X. P.; Wang, Y. Q.; Xiong, K.; Zhan, Z. P.; Jiang, Z.; Ding, Y. J. Xantphos doped Rh/POPs-PPh_3 catalyst for highly selective long-chain olefins hydroformylation: chemical and DFT insights into Rh location and the roles of Xantphos and PPh_3. *J. Catal*. **2017**, *353*, 123−132.

[4] Jia, X. F.; Liang, Z. Y.; Chen, J. B.; Lv, J. H.; Zhang, K.; Gao, M. J.; Zong, L. B.; Xie, C. X. Porous organic polymer supported rhodium as a reusable heterogeneous catalyst for hydroformylation of olefins. *Org. Lett*. **2019**, *21*, 2147−2150.

[5] Tan, M. H.; Yang, G. H.; Wang, T. J.; Vitidsant, T.; Li, J.; Wei, Q. H.; Ai, P. P.; Wu, M. B.; Zheng, J. T.; Tsubaki, N. Active and regioselective rhodium catalyst supported on reduced graphene oxide for 1-hexene hydroformylation. *Catal. Sci. Technol*. **2016**, *6*, 1162−1172.

[6] Shang, W. X.; Qin, B.; Gao, M. Y.; Qin, X. T.; Chai, Y. C.; Wu, G. J.; Guan, N. J.; Ma, D.; Li, L. D. Efficient heterogeneous hydroformylation over zeolite-encaged isolated rhodium ions. *CCS Chem*. **2023**, *5*, 1526−1539.

[7] Sun, G. C.; Fan, S. B.; Lv, J. M.; Zhao, T. S. Effective hollow Rh@H-S-1 catalyst for hydroformylation of 1-hexene. *J. Catal*. **2024**, *439*, 115770.

[8] Sun, G. C.; Chen, W.; Li, Y. Y.; Fan, S. B.; Lv, J. M.; Zhao, T. S. In situ synthesis of Rh@NaX catalyst for 1-hexene hydroformylation. *Fuel* **2024**, *373*, 132327.

[9] Feng, R.; Shen, J. M.; Wang, W.; Li, T. B.; Yan, X. L.; Lu, S. J. Enhancing regioselectivity through channel confinement in atomically dispersed Rh@S-1 catalyst for 1-hexene hydroformylation. *Chem. Eng. Sci*. **2026**, *320*, 122524.

[10] Yang, Y. H.; Tan, M. H.; Geng, H. L.; Gao, X. J.; Tan, Y. S.; Zhang, Q. D. Grafting EDTA in UiO-66 to modulate the microenvironment of Rh for 1-hexene hydroformylation. *Mol. Catal.* **2024**, *559*, 114100.

[11] Fang, Y.; Zhao, H.; Guo, X. Y.; He, Y. L.; Yang, G. H.; Tsubaki, N. Silicalite-1 encapsulated rhodium nanoparticles for hydroformylation of 1-hexene. *Catal. Today* **2023**, *410*, 150−156.

[12] Feng, R.; Wang, W.; Li, T. B.; Yang, F. F.; Hu, X. Y.; Yan, X. L.; Zhao, L. M.; Lu, S. J. Probing the distinct roles of zeolite-confined and external Rh sites by selective poisoning in regioselective 1-hexene hydroformylation. *Inorg. Chem. Front*. **2026**, *13*, 2413−2423.

Just Accepted